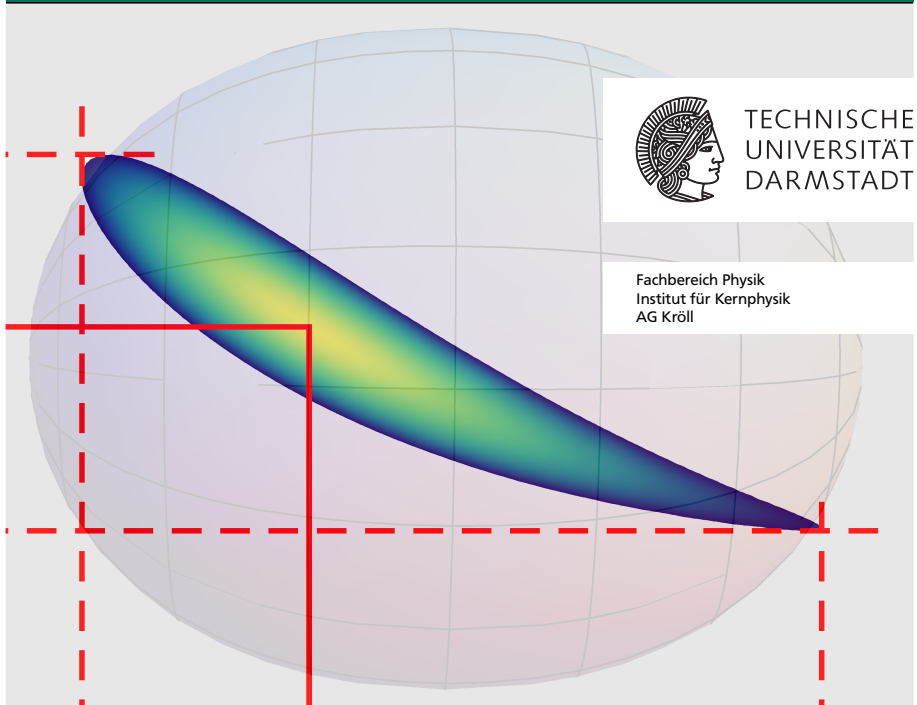


Quadrupole Collectivity in ^{128}Cd

Quadrupolkollektivität in ^{128}Cd

Vom Fachbereich Physik der Technischen Universität Darmstadt zur Erlangung des akademischen Grades eines Doktors der Naturwissenschaften (Dr. rer. nat.) genehmigte Dissertation von Esther Sabine Bönig M.Sc. aus Bünde 2014 – Darmstadt – D 17



TECHNISCHE
UNIVERSITÄT
DARMSTADT

Fachbereich Physik
Institut für Kernphysik
AG Kröll

IOLODE



Bundesministerium
für Bildung
und Forschung

HIC | FAIR
for

Helmholtz International Center

Quadrupole Collectivity in ^{128}Cd
Quadrupolkollektivität in ^{128}Cd

Vom Fachbereich Physik der Technischen Universität Darmstadt zur Erlangung des Grades eines Doktors der Naturwissenschaften (Dr. rer. nat.) genehmigte Dissertation von Esther Sabine Bönig M.Sc. aus Bünde

1. Gutachten: Prof. Dr. Thorsten Kröll
2. Gutachten: Prof. Dr. Joachim Enders

Tag der Einreichung: 05.06.2014

Tag der Prüfung: 07.07.2014

Darmstadt — D 17

Erklärung zur Dissertation

Hiermit versichere ich, die vorliegende Dissertation ohne Hilfe Dritter nur mit den angegebenen Quellen und Hilfsmitteln angefertigt zu haben. Alle Stellen, die aus Quellen entnommen wurden, sind als solche kenntlich gemacht. Diese Arbeit hat in gleicher oder ähnlicher Form noch keiner Prüfungsbehörde vorgelegen.

Darmstadt, den 05.06.2014

(S. Bönig)



*Face this world. Learn its ways, watch it,
be careful of too hasty guesses at its meaning.
In the end you will find clues to it all.*

H.G. Wells, *The Time Machine*



Abstract

The regions around shell closures, especially around doubly magic nuclei, are of major interest in nuclear structure physics, as they provide a perfect test for nuclear structure theory. The neutron-rich Cd isotopes in the region of ^{132}Sn are only two protons away from the shell closure at $Z = 50$ and in close proximity to the $N = 82$ magic number. Nevertheless they show an irregular behaviour regarding the excitation energy of the first excited 2^+ state. This is not reproduced by shell model calculations, which is astonishing due to the proximity of the shell closures. In order to shed light on the much discussed region around doubly magic ^{132}Sn , a Coulomb excitation experiment of ^{128}Cd has been performed at REX-ISOLDE, CERN. The reduced transition strength $B(E2; 0_{gs}^+ \rightarrow 2_1^+)$, which is a measure of collectivity, and the spectroscopic quadrupole moment $Q_s(2_1^+)$ as a measure of deformation could be determined for the first time. The results are shown as the continuation of already measured neutron-rich Cd isotopes and are compared to both beyond mean field and shell model calculations, which give different predictions for these observables.

Zusammenfassung

Die Gebiete um die Schalenabschlüsse, insbesondere nahe den doppelt-magischen Kernen, sind von grösstem Interesse für die Kernstrukturphysik, da sie einen perfekten Test für Kernstrukturtheorien darstellen. Die neutronenreichen Cd Isotope nahe ^{132}Sn sind lediglich zwei Protonen von dem Schalenabschluss bei $Z = 50$ entfernt und unweit der magischen Zahl $N = 82$. Trotzdem zeigen sie ein irreguläres Verhalten in der Anregungsenergie des ersten 2^+ Zustandes. Dieses wird von den Schalenmodellrechnungen nicht reproduziert, was erstaunlich ist, da die Schalenabschlüsse in unmittelbarer Nähe liegen. Um Licht in das Gebiet um ^{132}Sn zu bringen, wurde ein Coulombanregungsexperiment von ^{128}Cd bei REX-ISOLDE, CERN durchgeführt. Die reduzierte Anregungsstärke $B(E2; 0_{gs}^+ \rightarrow 2_1^+)$, die eine Messgröße der Kollektivität darstellt, und das spektroskopische Quadrupolmoment $Q_s(2_1^+)$ als Messgröße der Deformation konnten zum ersten Mal bestimmt werden.

Die Ergebnisse werden als Weiterführung der schon gemessenen neutronenreichen Cd Isotope gezeigt und mit “beyond mean field” und Schalenmodellrechnungen verglichen, die unterschiedliche Vorhersagen für diese Observablen liefern.

Contents

1. Introduction	1
1.1. Historical overview	1
1.2. Motivation	2
2. Nuclear structure physics	7
2.1. Collective model	8
2.2. Shell model	11
2.2.1. Spherical shell model	11
2.2.2. Deformed shell model - The Nilsson model	15
2.3. Mean field theory and beyond	17
3. Low-energy Coulomb excitation	19
3.1. The semi-classical description	19
3.2. First order perturbation theory	22
3.2.1. First order effects	22
3.2.2. Second order effects	24
3.3. Computation of Coulomb excitation cross sections - the CLX/DCY code	25
4. The REX-ISOLDE facility and MINIBALL	27
4.1. Beam production and extraction	27
4.2. Post acceleration	28
4.3. Experimental area - MINIBALL	31
4.3.1. Particle detection	31
4.3.2. γ -ray detection	33
5. Experimental details	37
5.1. Beam and target details	37
5.2. Calibrations and corrections	39
5.2.1. Energy and efficiency calibration	40
5.2.2. HPGe-detectors	41
5.2.3. DSSSD	42
5.2.4. Doppler correction	44



6. Data analysis	45
6.1. Beam purity	47
6.1.1. Identification of contaminants	47
6.1.2. ^{128}Cs contamination	48
6.1.3. ^{128}In and ^{128}Sn contamination	50
6.2. Coulomb excitation analysis	60
6.2.1. Details on ^{128}Cd	64
6.2.2. Details on ^{128}In	65
7. Results, discussion and outlook	73
7.1. Results and discussion	73
7.2. Outlook	78
A. Kinematical reconstruction	83
Bibliography	85
List of figures	90
List of tables	93
List of Publications	94
Curriculum Vitae	95

1 Introduction

1.1 Historical overview

In 1909 H. Geiger and E. Marsden performed under the direction of E. Rutherford an experiment [Gei09], whose outcome should open up a new field of physics. They investigated the scattering of an α -particle beam on a gold foil. It was, however, in 1911 that E. Rutherford interpreted the results of this experiment and drew the conclusion, that *“the atom consists of a central charge supposed concentrated at a point”* [Rut11] - today known as the atomic nucleus. It was then some experiments later in 1918, that the proton was discovered by Rutherford as the particle carrying this central positive charge. Around the atomic nucleus, negative charges - the electrons - were thought to move along orbits. The introduction of discrete energy levels for the electrons was done by N. Bohr in 1913, when he postulated a modified atomic model. This was able to explain the spectral lines specific for atoms first discovered in the sun by W.H. Wollaston in 1802 [Wol02] and J.v. Fraunhofer in 1814 [Fra14] and further investigated by G. Kirchhoff and R. Bunsen [Kir60]. The limitations of Bohr’s atomic model lie amongst others in the prediction of the ground state angular momentum and the description of the spectral lines of heavy atoms. These shortcomings lead to a new theory developed by W. Heisenberg, M. Born and P. Jordan and was introduced in 1925 as a whole new mathematical description of the atom - quantum mechanics [Hei25, Bor25, Bor26]. It was, however, years later in 1932, that the constituents of the already discovered atomic nucleus could be pinned down by the discovery of the neutron by J. Chadwick [Cha32]. The crucial experiment was that by Bothe and Becker in 1930, which revealed a penetrating but not ionising radiation out of the nucleus after bombardment with α -particles [Bot30]. With this discovery it was possible for the first time to extract the binding energy of a nucleus by comparing its total mass with the masses of the constituting particles. The theoretical description of the neutron was formulated by W. Heisenberg also in 1932, explaining the symmetry between protons and neutrons [Hei32]. It was then only later in 1937 that the name of the quantum number - the isospin - was introduced by E. Wigner [Wig37]. With the introduction of an attractive force between the protons and neutrons, the nuclear force, it eventually was possible to explain the binding of those into an

atomic nucleus. The potential introduced by and later named after Yukawa was in 1935 the first theoretical description of this force [Yuk35]. It included a new particle mediating the interaction between the nucleons. This particle was first guessed to be the μ lepton, but later discovered as the π meson. Nowadays it is known, that the nuclear force is only a residual part of the more fundamental interaction between more elementary particles, the strong force acting between the quarks. The quarks were first proposed by M. Gell-Mann [Gel64] and G. Zweig [Zwe64] in 1964. The first experimental evidence was then found in a deep inelastic scattering experiment at the Stanford Linear Accelerator Center in 1968 [Blo69, Bre69].

Today more than 3000 different nuclei are known with less than 300 of them being stable. They are characterised by their proton and neutron number Z and N and mass number A : ${}^A_Z X_N$, with X being the element symbol. All these nuclei are sorted in the nuclear chart according to their nucleon numbers (fig. 1.1). As more and more nuclei became known and experimentally accessible, their nuclear properties like half lifes, masses, radii, electric and magnetic moments were studied in various different experiments. New nuclear models were developed and further extended in order to reproduce the experimental values and to gain new information about the properties of the strong force between the nucleons and their effect on the nuclear structure. It is only since the past few years that exotic nuclei, that is nuclei with extreme N/Z ratios, became experimentally accessible. But exactly these highly unstable nuclei show interesting and extraordinary phenomena, providing a perfect test for different nuclear structure theories.

1.2 Motivation

One example of those highly exotic nuclei that became experimentally accessible is the heavy and neutron-rich ${}^{128}\text{Cd}$ near the $N = 82$ and $Z = 50$ shell closures, where only scarce information exist. A quenching of the shell gap at $N = 82$ has already been proposed 20 years ago by Dobaczewski et al. [Dob94]. This would express itself in an increase in quadrupole collectivity compared to an unquenched shell gap. However, so far no definite experimental evidence was found. By the investigation of ${}^{128}\text{Cd}$, which is only two proton and two neutron holes away from the shell closures (fig. 1.2), in a Coulomb excitation experiment the transition strength from the 0^+ ground state to the first excited 2^+ state can be determined and gives insight to the question of shell gap quenching. A unique anomaly in the Cd isotopic chain has been discovered by the measurement of the energy of the first excited 2^+ state. The increase towards the $N = 82$ shell closure is not at all as steep as in the neighbouring isotopes like ${}_{52}\text{Te}$ and ${}_{46}\text{Pd}$, for example, and even decreases from ${}^{126}\text{Cd}$ to ${}^{128}\text{Cd}$, as is depicted in figure 1.3. The 2^+ energy for ${}^{128}\text{Cd}$ is with 646 keV

even lower than for both $N = 80$ isotones $^{132}_{52}\text{Te}$ ($E(2^+_1) = 974$ keV [Ker74]) with four protons more and the recently measured $^{126}_{46}\text{Pd}$ ($E(2^+_1) = 693$ keV [Wat13]) with two protons less than ^{128}Cd . Another peculiarity was found in ^{136}Te , which has two protons and two neutrons more than the doubly magic ^{132}Sn (instead of having two proton and neutron holes like ^{128}Cd) [Rad02, Dan11]. The transition strength from the ground to the first excited state is less than expected by shell model calculations. Neither the findings of the anomaly in the excitation energies of the Cd isotopes nor the low transition strength in ^{136}Te are reproduced with shell model calculations, which is astonishing as the proton and neutron shell closures are both in close proximity.

An understanding of the Cd isotopic chain, and especially ^{128}Cd , will as well influence nuclear astrophysics. The path of the astrophysical r-process, which is the rapid neutron capture, passes near ^{128}Cd and is responsible for the nucleosynthesis of heavy (heavier than ^{56}Fe) neutron-rich nuclei in *e.g.* supernova explosions. The description of the solar abundance peak at around $A \simeq 130$ is improved assuming a $N = 82$ shell gap quenching [Che95]. However, the lack of experimental information on most of the r-process nuclei requires theoretical extrapolations in order to investigate the nucleosynthesis. With this very first measurement of the transition strength from the 0^+ ground state to the first excited 2^+ state, which acts as a measure of quadrupole collectivity, in ^{128}Cd , the understanding of the nuclear structure in this region is improved.

This work will at first (chapter 2) discuss basic considerations of nuclear structure physics, including the ideas of shell model (SM) and beyond mean field (BMF) theory, in order to be able to interpret the results of the performed experiment. In chapter 3 the method used for the investigation of ^{128}Cd - low energy Coulomb excitation - is explained and the connection between theoretical description and experimental observables is drawn. This is followed by a description of the beam production and acceleration at REX-ISOLDE, CERN, and the experimental setup MINIBALL in chapter 4. Chapter 5 deals with the corrections and calibrations performed in order to analyse the obtained experimental data. This analysis is explained in great detail in chapter 6, where as well the handling with the beam contamination is addressed. The outcome of the experiment is summarised and discussed in the vicinity of shell model and beyond mean field calculations in chapter 7, where as well an outlook for further investigations is given.

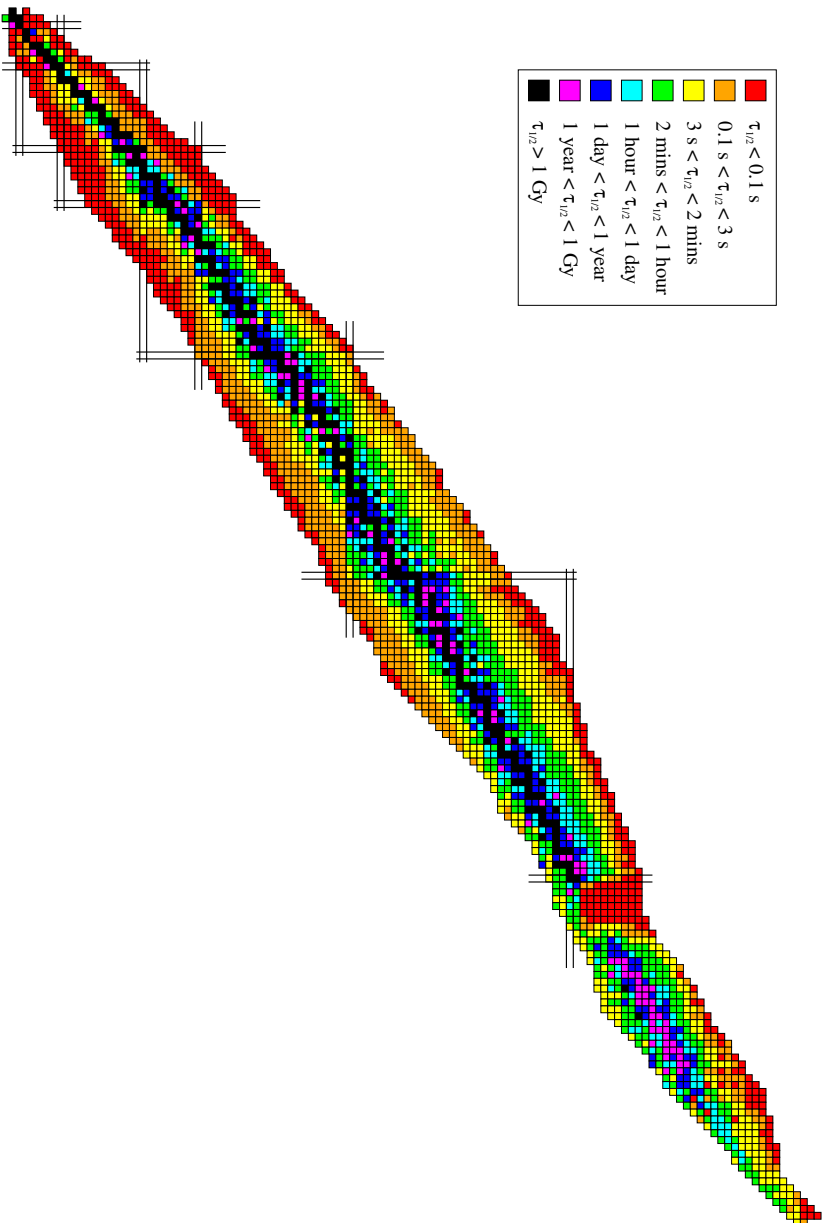


Figure 1.1.: Nuclear chart. Color coded is the lifetime of the ground state of the nuclei. The magic numbers (black encapsulating strips) are indicated. Figure is generated with *inch* [Inc14].

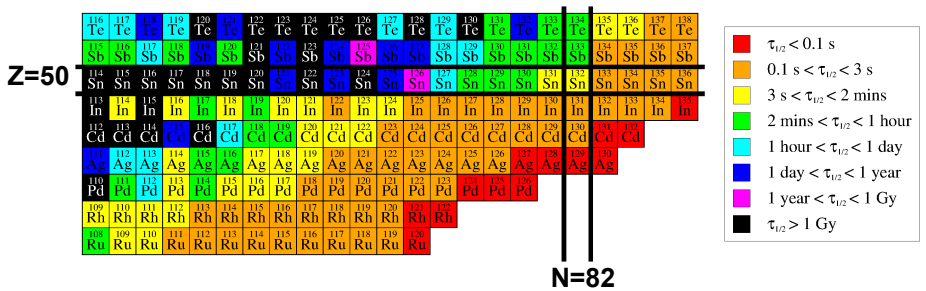


Figure 1.2.: Region around ^{128}Cd with indicated shell closure at $N = 82$ and $Z = 50$. Color coded is the lifetime of the ground state of the nuclei. Figure is generated with *inch* [inc14].

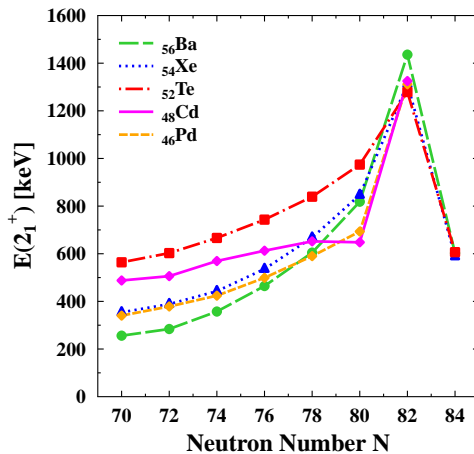


Figure 1.3.: Excitation energies of the first excited 2^+ state in different isotopes. Note the less steep increase in the Cd isotopic chain towards the $N = 82$ shell closure.



2 Nuclear structure physics

One of the first attempts to describe the atomic nucleus was done analogous to the atomic shell model. In 1932 D. Ivanenko and E. Gapon proposed to describe the nucleus in terms of energy levels and orbitals [Gap32]. The nuclear shell model (SM) was then formulated and further developed independently by M. Goepfert-Mayer [Goe49] and J.H.D. Jensen [Hax49], who were awarded the nobel prize in 1963 “*for their discoveries concerning nuclear shell structure*” [nob14]. The basic idea of the nuclear shell model is, that the nucleons are distributed on shells with a certain energy and satisfy the Pauli exclusion principle like the electrons in an atom. In contrast to atomic physics, where the electromagnetic interaction plays the major role, the nucleons underly also the strong interaction. It was found experimentally, that nuclei with certain proton and neutron numbers, today known as the “magic numbers” (2, 8, 20, 28, 50, 82, 126), do not follow the semiempirical mass formula by C.F. von Weizsäcker [vW35]. These nuclei are much more bound compared to their neighbours. The first formulation of the shell model was able to reproduce this finding up to $N, Z = 20$, but needed to be revised in order to also account for the higher numbers. Therefore Goepfert-Mayer and Jensen improved their first formulation of the shell model by including the spin-orbit coupling, which turns out to be much larger than in atoms. However, also these improvements could not explain further observations like enhanced quadrupole moments, *i.e.* large quadrupole deformation, and large transition probabilities for nuclei with many valence nucleons away from magic numbers and closed shells. These limitations of the shell model lead to the description of the nucleus within another approach - the collective model introduced by A. Bohr and B.R. Mottelson [Boh58]. It was discovered that the origin of such enhanced values lies in a collective behaviour of the nucleons and that the nucleus in these regions can not be described by simple one-nucleon excitations. Nevertheless, the properties of the nuclei can not be explained by SM or collective models exclusively, but rather need features from both theories. The single particle orbits described by the shell model depend on the form of the nuclear potential, described by the wave functions calculated within the framework of a collective model. In this chapter the ideas of the collective model as well as the basic and state-of-the-art shell model will be described. Furthermore the coupling of both theories to the deformed shell model will shortly be outlined. At last, a modern numerical mean field approach is sketched.

2.1 Collective model

Experimental evidences lead to the development of a collective model, in which the nucleons exhibit a collective motion, that means they move coherently with well-defined phases. Different types of collective motions like vibration and rotation exist. These show for even-even nuclei typical structures in their excitation spectrum and will be discussed further, before a brief mathematical description of the collective model follows.

Vibration: The excitation quanta for a vibration are called phonons. Each phonon carries $\lambda\hbar$ angular momentum and parity $\pi = (-1)^\lambda$, with λ being the multipole order. In even-even nuclei the 0-phonon state represents the ground state, whereas the first excited state is formed by a one-phonon excitation. For quadrupole phonons with $\lambda = 2$ the first excited one-phonon state is a 2^+ -state. A coupling of two quadrupole phonons results in three states ($0^+, 2^+, 4^+$) at twice the energy of the one-phonon excitation (fig. 2.1, left). For a Hamiltonian including only vibrational terms, that is a harmonic oscillator, those three states would be degenerate in energy. However, the non-vanishing residual interaction between the phonons splits the states to different energies. A good test to decide whether a nucleus is a typical vibrator or not, is the ratio R_{42} of the energies of the first excited 4^+ - and 2^+ -state:

$$R_{42} = \frac{E(4_1^+)}{E(2_1^+)} = 2. \quad (2.1)$$

In case this ratio has the value 2 the nucleus can be considered a typical vibrator. Another characteristic of a vibrational nucleus is the probability for an E2-transition. This should be twice as large for the decay of two-phonon states than for a one-phonon state into the ground state. For a long time it was thought that a good example for vibrational nuclei is found in the Cadmium isotopic chain. The stable Cd isotopes show the typical energy spectrum of a vibrator. However, when these nuclei became available in recent experiments addressing the transition probabilities [Gar08], the values did not follow the predictions. Garrett et al. [Gar08] then drew the conclusion, that the stable Cd isotopes may not represent a perfect vibrational system.

Rotation: Rotational modes can only be found in nuclei, which have a deformed shape, *i.e.* away from shell closures. With the assumption of a rigid nucleus it is

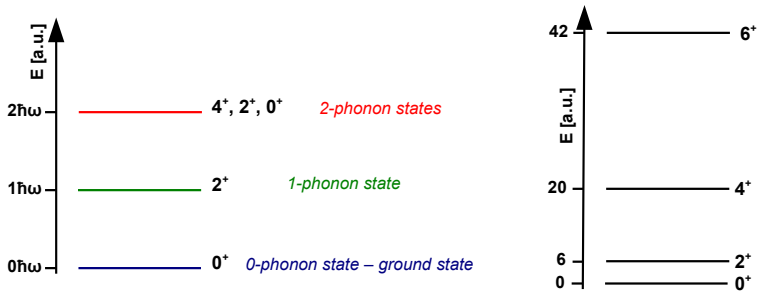


Figure 2.1.: Schematic view of the excitation energies in a spherical quadrupole vibrational nucleus without residual interactions (left) and in a deformed rotational nucleus according to equ. 2.4 (right).

described as an axially symmetric system rotating along an axis perpendicular to the symmetry axis. The Hamiltonian

$$H = \frac{\hbar^2}{2\Theta} \cdot \vec{I}^2 \quad (2.2)$$

consists of the moment of inertia Θ with respect to the rotation axis and the sum \vec{I} of angular momentum generated by the core rotation and the intrinsic angular momentum of the unpaired valence nucleons. The projection of \vec{I} onto the symmetry axis is given by a new quantum number K . Solving the Schrödinger equation leads to the energy eigenvalues

$$E_{\text{rot}} = \frac{\hbar^2}{2\Theta} [J(J+1) - K^2] \quad (2.3)$$

with the total angular momentum J . This leads to the energies of the first excited states

$$\begin{aligned} E(2_1^+) &= 6 \frac{\hbar^2}{2\Theta}, \\ E(4_1^+) &= 20 \frac{\hbar^2}{2\Theta}, \\ E(6_1^+) &= 42 \frac{\hbar^2}{2\Theta}, \end{aligned} \quad (2.4)$$

which is sketched in fig. 2.1, right. The typical rotor has a value of $R_{42} = 3.33$. Most examples of such typical rotors are found in the rare-earth region and the actinides.

To describe the collective motion of nucleons mathematically, it is convenient to introduce collective coordinates $a_{\lambda\mu}$, which describe the vibration of a nucleus relatively to its ground state. In nature most nuclei do not exhibit vibrational or rotational modes alone, but rather a mixture of both, which is described by the general collective model. We will in the following discuss only the basic structure of a collective model as found in [Eis75]. Details on the general collective model can be found in [Hes80]. The nuclear surface can be expanded into spherical harmonics $Y_{\lambda\mu}$ and written in terms of the collective coordinates

$$R(\theta, \phi, t) = R_0 \left(1 + \sum_{\lambda, \mu} (-1)^\mu a_{\lambda, -\mu}(t) Y_{\lambda, \mu}(\theta, \phi) \right), \quad (2.5)$$

with R_0 being the radius of a spherical nucleus, for which the $a_{\lambda\mu}$ vanish. The vibrational modes can be classified in terms of multipole order λ . The monopole term ($\lambda = 0$) corresponds to the breathing mode, which is the change of volume of the nucleus. Due to the relatively high incompressibility of nuclear matter, these excitations lie at very high energies (a couple of tens of MeV). The static dipole term ($\lambda = 1$) describes a center of mass motion, that is a translation of the nucleus. The dynamical dipole term gives the giant dipole resonance. In the context of this work the most interesting term is the quadrupole term with $\lambda = 2$, which corresponds to the quadrupole deformation (static) and its change (dynamic) of the nucleus. Considering only the static quadrupole term, equ. 2.5 can be written as

$$R(\theta, \phi) = R_0 \left(1 + \sum_{\mu} a_{2, \mu}^* Y_{2, \mu}(\theta, \phi) \right), \quad (2.6)$$

with the condition $a_{\lambda, \mu}^* = (-1)^\mu a_{\lambda, -\mu}$. Expressing the sum in cartesian coordinates, it is immediately clear that the $a_{2, \mu}$ describe the shape of the nucleus (see for further information [Eis75]). A transformation to an instantaneous principal axis system, which is rotated by the Euler angles with respect to the laboratory-fixed system, gives $a_{2, \pm 1} = 0$. The components $a_{2, 0}$ and $a_{2, 2} = a_{2, -2}$ lead to the intrinsic nuclear shape, whereas the Euler angles indicate the rotation of the nucleus. Bohr and Mottelson [Boh53] introduced the nowadays better known parameters β and γ

$$\begin{aligned} a_{2, 0} &= \beta \cos(\gamma), \\ a_{2, 2} &= \frac{\beta}{\sqrt{2}} \sin(\gamma), \end{aligned} \quad (2.7)$$

with

$$\sum_{\mu} |a_{2, \mu}|^2 = \beta^2. \quad (2.8)$$

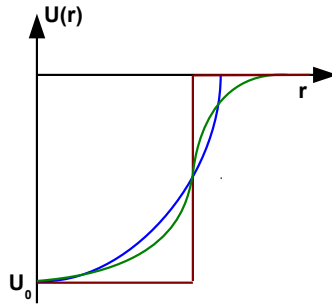


Figure 2.2.: A sketch of the square well potential (red), the harmonic oscillator potential (blue) and the Woods-Saxon potential (green) with depth U_0 .

The parameter β refers to the deviation from spherical symmetry. The triaxiality parameter γ represents the deviation from rotational symmetry, that is axial deformation, and can be visualised as a stretching of the nucleus perpendicular to the symmetry axis. However, two different conventions for the parameters exist. A common convention is, that γ can take values from 0° to 30° , where $\gamma = 0^\circ$ and $\gamma = 30^\circ$ correspond to axially symmetric nuclei. Then the sign of β gives the type of deformation - $\beta > 0$ for a prolate and $\beta < 0$ for an oblate shape. In another convention γ can take values between 0° and 60° , where $\gamma = 0^\circ$ corresponds to an axially symmetric oblate nucleus and $\gamma = 60^\circ$ describes an axially symmetric prolate nucleus. Here β only takes positive values.

2.2 Shell model

2.2.1 Spherical shell model

To describe the nucleus within the shell model approach, a spherically symmetric nucleon-nucleon potential $V_{ij}(r)$ with $r = |\vec{r}|$ is used. Higher order interactions like three-body forces are neglected at this point. The Hamiltonian can be written as the sum of the kinetic energies of the particles and the interaction potential $V_{ij}(r)$

$$H = \sum_{i=1}^A T_i + \sum_{i < j=1}^A V_{ij}(r) = \underbrace{\sum_{i=1}^A \left(\frac{\vec{p}_i^2}{2m_i} + U(r_i) \right)}_{H_0} + \underbrace{\sum_{i < j=1}^A V_{ij}(r) - \sum_{i=1}^A U(r_i)}_{H_{res}}. \quad (2.9)$$

By introducing a central mean field potential $U(r)$ created by the nucleons ($U(r_i)$ is the mean potential acting on a nucleon i created by the surrounding nucleons up to a certain distance), the Hamiltonian can be divided into two parts: 1) A part H_0 describing the independent single particle motion of the nucleons in the mean field potential, which will build the shell structure (*i.e.* single particle energies) and 2) the residual interaction H_{res} , which will be responsible for the details of the nuclear structure. The mean potential $U(r)$ needs to have sharp boundaries, as the strong force is only very short ranged. An appropriate choice would either be a square well or an harmonic oscillator potential

$$U(r) = -U_0 + \frac{m}{2} \omega^2 r^2, \quad (2.10)$$

with a depth U_0 , nucleon mass m , oscillator frequency ω and radius r . In order to reproduce the experimentally found magic numbers, Goeppert-Mayer [Goe49] and Jensen [Hax49] processed - independently from each other - the idea to include one more term in the potential: $\vec{l} \cdot \vec{s}$ for the interaction of spin and angular momentum. Because the calculated energy of the orbitals with large angular momentum \vec{j} were found to be too high, another term, $C\vec{l}^2$, has been introduced. Therefore the modified potential reads

$$U(r) = -U_0 + \frac{m}{2} \omega^2 r^2 + C\vec{l}^2 - D\vec{l} \cdot \vec{s}. \quad (2.11)$$

The parameter C characterises the deviation from an harmonic oscillator potential and is negative. The constant D represents the strength of the spin-orbit coupling and is negative for the coupling $j = l - 1/2$ and positive for $j = l + 1/2$. Both parameters have to be determined empirically. However, a more realistic potential is a potential between the square well and the harmonic oscillator, already referred to by Goeppert-Mayer and Jensen [Goe55]. Therefore Woods and Saxon created such a potential, called the Woods-Saxon potential [Woo54] (see fig. 2.2)

$$U(r) = -\frac{U_0}{1 + \exp[(r - R)/a]} \quad (2.12)$$

with a depth U_0 , the radius R and the skin thickness a . The quantum numbers n (radial, $n = 1, 2, 3, \dots$), l (orbital, $l = 0, 1, \dots, n - 1$), s (spin, $s = \pm 1/2$) and j (total angular momentum, $j = l + s$) are introduced to classify the different shells. By solving the Schrödinger equation $H\Psi = E\Psi$ for the shell model Hamiltonian (equ. 2.9) the different shells can be calculated. Note, that in a non-relativistic treatment this is only possible analytically for the square well and harmonic oscillator potential, but not for the Woods-Saxon potential. Figure 2.3 shows the effect

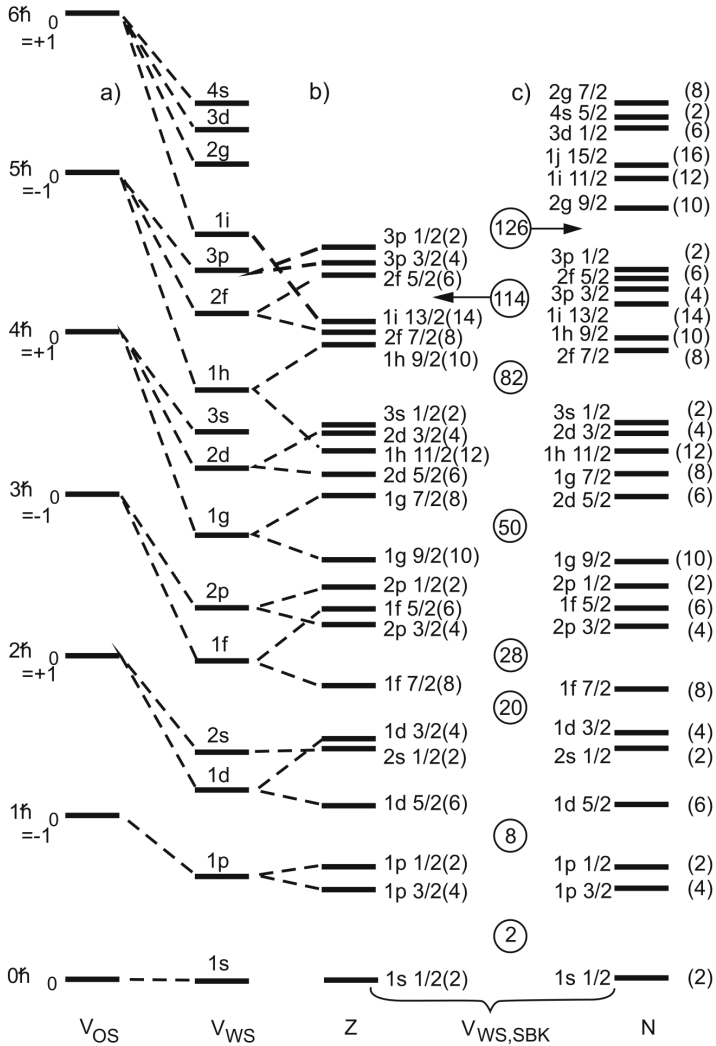


Figure 2.3.: Shell model levels for the harmonic oscillator (V_{OS}), Woods-Saxon (V_{WS}) and Woods-Saxon potential with spin-orbit coupling for protons Z and neutrons N separately ($V_{WS,SBK}$). Figure taken from [Bet08].

of the choice of the different potentials and the inclusion of the additional terms on the orbitals.

Modern descriptions of nuclei in the vicinity of the shell model use a basis of harmonic oscillator states to solve the A -body Schrödinger equation including the shell model Hamiltonian (equ. 2.9) and preserves all underlying symmetries. This Schrödinger equation can, in general, not be solved exactly. Therefore the realistic interaction amongst the nucleons is described by effective interactions. These are either determined purely empirically by fitting to experimental data, or obtained microscopically from models like coupled cluster theory. In first order, only NN potentials are taken into account. The inclusion of 3-body interactions was first done in 2002 by D.C.J. Marsden et al. [Mar02] and is nowadays common practice. With these effective interactions the many-body Hamiltonian can be diagonalised, and observables like excitation spectra, transition strengths and quadrupole moments can be calculated. This method, where all the nucleons are treated as being active, is only applicable for light nuclei with $A \lesssim 18$ and is called the No Core Shell Model (NCSM) [Nav00]. More detailed information can be found in [Bar13]. For heavier nuclei the model space becomes too large and the diagonalisation of the Hamiltonian is no longer possible due to a significant growth in computing time. Being able to perform calculations for nuclei throughout the nuclear chart needs a reduction of the model space. Up to now three different approaches are capable to do so: The importance truncation approach [Rot07], the NCSM in the framework of an effective field theory [Ste07] and the standard SM with a core [Lis08]. In the following only the latter method will shortly be discussed. In the standard SM with a core the model space is reduced by dividing the nucleus into an inert core and interacting valence nucleons. The inert core is chosen to be the nucleus with proton and neutron magic numbers nearest to the nucleus of interest. The core consists of only fully-occupied shells from where no excitations are allowed in leading order. Therefore the effective interaction is obtained only for the valence nucleons and the Hamiltonian for those can be diagonalised. The fully closed shells have a spherical shape, whereas the unfilled valence shells can deform the nucleus. For the special case that there is only one nucleon in the valence shell, there are no interactions between valence nucleons. Then the occupied orbit completely describes the ground state energy and spin of the whole system. For more than one valence nucleon the interaction between those has to be taken into account. It is described by the residual interaction H_{res} , which in even-even nuclei mostly consists of pairing forces acting between the single nucleons.

The spherical shell model is very successful in describing ground state spins, parities and magic numbers. But when it comes to mid-shell nuclei and its phenomena

like quadrupole deformation, shell model predictions do not fit the experimental results very well. Most of the measured quadrupole moments and transition probabilities are much larger than expected from single-nucleon transitions. It seems that the spherical mean field approach is no longer appropriate when it comes to off-shell phenomena.

2.2.2 Deformed shell model - The Nilsson model

In order to account for a deformation of a nucleus, a special model was developed to describe single particle energies with respect to a deformed mean potential. The model is called the Nilsson Model or the deformed shell model. In 1955 S.G. Nilsson introduced a modified Hamiltonian, which describes a single particle moving in an axially deformed harmonic oscillator potential with spin-orbit coupling [Nil55]

$$H = \frac{\vec{p}^2}{2m} + \frac{m}{2} \left(\omega_x^2 (x^2 + y^2) + \omega_z^2 z^2 \right) + C\vec{l}^2 - D\vec{l} \cdot \vec{s} \quad (2.13)$$

The oscillating frequencies

$$\begin{aligned} \omega_{x,y} &= \omega_0(\varepsilon)(1 + 1/3\varepsilon), \\ \omega_z &= \omega_0(\varepsilon)(1 - 2/3\varepsilon), \end{aligned} \quad (2.14)$$

are written as a function of the deformation parameter ε . The quantity $\omega_0(\varepsilon)$ is given as

$$\omega_0(\varepsilon) = \omega_0 \left[1 + 1/9\varepsilon^2 + \mathcal{O}(\varepsilon^3) \right] \quad (2.15)$$

where ω_0 is the value of ω_0 at $\varepsilon = 0$. Note that the deformation parameter ε is connected to the deformation parameter β used by Bohr and Mottelson for the collective model (eq. 2.7) to first order via the approximation

$$\varepsilon \simeq 3/2 \sqrt{\frac{5}{4\pi}} \beta + 3/8 \frac{5}{4\pi} \beta^2 + \mathcal{O}(\beta^3). \quad (2.16)$$

Figure 2.4 shows the single-particle energy levels for protons and neutrons with respect to the deformation parameter δ . Note, that the relation $\varepsilon = \delta + \frac{1}{6}\delta^2 + \mathcal{O}(\delta^3)$ holds [Nil55].

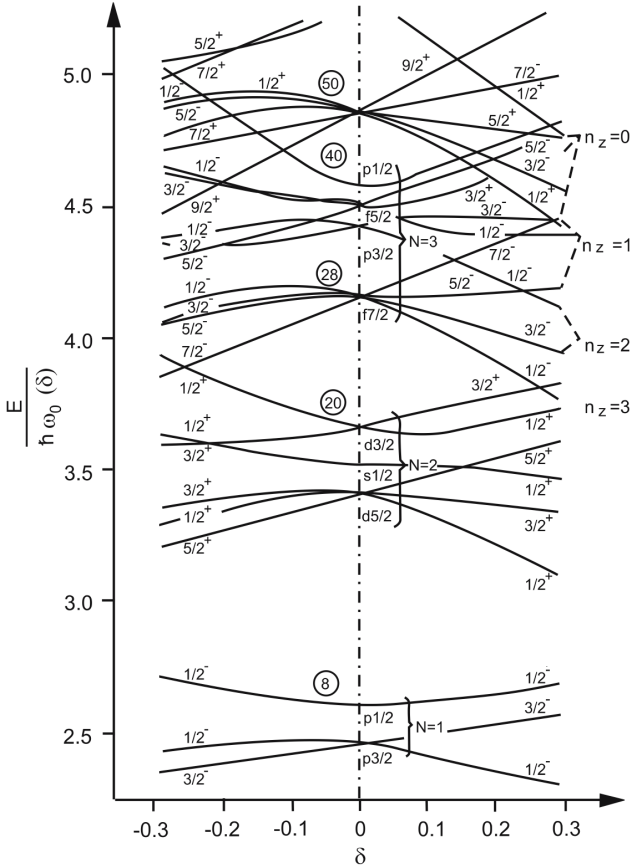


Figure 2.4.: Deformed shell model levels for proton and neutrons following the formulation by Nilsson. Note, that $\varepsilon = \delta + \frac{1}{6}\delta^2 + \mathcal{O}(\delta^3)$ [Nil55]. The asymptotic (only good for large deformation) quantum number n_z is the number of nodes in the wave function in z-direction. For levels in a shell N and angular momentum $J = 1/2$ the quantum number $n_z = N$ for the lowest level and $n_z = N - 1$ for the next etc. For angular momentum $J = 3/2$ the quantum number $n_z = N - 1$ for the lowest level and $n_z = N - 2$ for the next and so on. The quantum number Ω is the projection of the angular momentum onto the symmetry axis. The value Ω^π is indicated for each level. Figure taken from [Bet08].

2.3 Mean field theory and beyond

The Nilsson model describes nuclei in the vicinity of the single particle model very well, but in order to describe the nuclear properties even better, a treatment of more realistic potentials is needed. An approach besides SM to describe nuclear properties is the mean field method [Ben03], also known as self-consistent field theory, which uses the framework of quantum field theory. The mean field is derived from effective interactions using a Hartree-Fock (HF) approach in a self-consistent way. In this approach the total N -body wave function $|\Phi\rangle = a_{k_1}^\dagger \dots a_{k_N}^\dagger |0\rangle$, with $a_{k_i}^\dagger$ being the creation operators for nucleons in the orbit k , is constructed from the shell model Hamiltonian (equ. 2.9). After the minimisation of the obtained Hartree-Fock energy with the constraint of a fixed number of multipole moments a mean field is obtained. Iterating this procedure leads to a stable solution for the mean field [Ber07]. However, the Hartree-Fock method can only be applied if the long range components of the nucleon-nucleon interaction, which cause particle-hole correlations and contribute to the nuclear deformation, dominate the short range ones, which cause particle-particle correlations and serve as origin for pairing correlations. In order to account for the short range interaction, the Hartree-Fock + Bardeen-Cooper-Schrieffer (HF + BCS) approach [Bar57] can be used, where the pairing interaction is included in the Hamiltonian. The approximate solution leads to the BCS-states, whose probability of occupation can be determined. Note that for these states an occupation above the Fermi level is possible. A drawback of this method is that the particle number is not conserved. To overcome this problem, Bogolyubov and Valatin developed a method by transforming the creation and annihilation operators to new quasi-particle operators. This leads to the so-called HFB equations [Bog58, Val58]. Solving these equations leads to the construction of the corresponding wave functions $|\Phi\rangle$. The intrinsic state can break different symmetries of the system, which have to be restored in order to produce physical states. This is done by the projection of these intrinsic states onto the quantum number corresponding to the broken symmetry (*i.e.* fixed particle number, isospin, angular momentum). The success of the calculation of the mean field is highly dependent on the choice of the interaction. The first attempts for the calculation of this interaction was made directly from the bare nucleon-nucleon potential by Muthukrishnan and Baranger in 1965 [Mut65]. But to describe the nuclei on a quantitative level an effective interaction had to be introduced. The two main non relativistic effective interactions are the Skyrme [Sto06] and the Gogny interaction [Dec80]. The Skyrme functional describes the nucleon-nucleon potential by a contact force, whereas Gogny is a finite range interaction. The finite range interaction has the advantage, that pairing correlations do not need to be put

in as an adjustable parameter but are included self-consistently. This reduces the number of available parametrisations for the Gogny functional significantly. Both interactions are considered phenomenological, as they are adjusted to experimental data like masses and radii on a global level. A third very important effective interaction within the mean-field theory is the relativistic mean field [Rei89]. In this approach the nucleons are described by Dirac spinors from which the many-body state is built and the motion of nucleons is given by the Dirac equation. The nucleons interact through a finite-range meson field, the simplest exchange meson being the pion. The effective interaction of the meson fields is described with the Klein-Gordon equation. The advantage of the relativistic mean field model compared to the Gogny and Skyrme effective interaction is the natural outcome of relativistic effects like the spin-orbit coupling.

In order to describe the nuclear properties with a higher precision, additional methods can be applied to the mean field theory. These additional methods then include correlations as, for example, collective motion. These can be considered by applying different methods, one being the generator coordinate method (GCM) [Tab72, Rei87]. It is based on the variational principle and combines collective motion and single particle effects. In the GCM the basis is formed by the BCS or HFB states and the wave functions $|\Phi(q)\rangle$ are constructed depending on the collective coordinate q . The energy can be calculated with the variational principle, where the variation is either performed before or after the projection of the states onto quantum number of the broken symmetry. The collective coordinate can be chosen such that it restores the broken symmetries or includes shape degrees of freedom. Through this parameter, information about the quadrupole deformation is gained.

3 Low-energy Coulomb excitation

With the development of radioactive beams, the investigation of nuclear properties for nuclei away from stability became possible. This important step and the interplay between theoretical and experimental physics lead to an extended understanding of nuclear matter even though open questions still arise. However, the production and delivery of a radioactive beam to the actual experiment is not at all trivial, as each single nucleus needs to be produced in a nuclear reaction and many of the unstable nuclei decay within fractions of a second [Gla09]. Therefore the yields of such beams are much less compared to stable beam experiments, which makes the choice of the experimental method for the investigation of an unstable nucleus even more crucial. One of these methods of choice is Coulomb excitation. In such experiments a radioactive ion beam (RIB) is shot on a target material and is scattered inelastically. Both scattering partners can get excited by exchanging a virtual photon. The trajectory of the incoming particle in the Coulomb field of the scattering target nucleus can be described classically if the beam energy is sufficiently low, whereas the excitation process can only be described quantum mechanically. In this chapter this so-called semi-classical description will be explained and the connection between theory and experimental observables will be drawn.

3.1 The semi-classical description

The inelastic scattering of a beam at a target nucleus is a purely electromagnetic process and therefore well described by theory, if the beam energy is sufficiently low, *i.e.* well below the Coulomb barrier V_C

$$V_C = \frac{e^2}{4\pi\epsilon_0} \frac{Z_p Z_t}{R_p + R_t}, \quad (3.1)$$

with $R_i \propto 1.25 \cdot A_i^{1/3}$ being the radius of the projectile and target nucleus, respectively. The maximum “safe” collision energy E_{\max} is given as

$$E_{\max}(\Theta_{cm}) = 0.72 \cdot \frac{A_p + A_t}{A_t} \cdot \frac{Z_p Z_t}{D_{\min}} \left(1 + \frac{1}{\sin(\Theta_{cm}/2)} \right) [\text{MeV}], \quad (3.2)$$

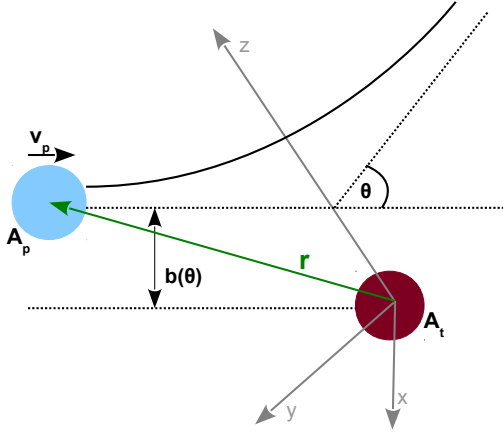


Figure 3.1.: Schematic view of low-energy Coulomb scattering.

with D_{\min} being the distance of closest approach. To ensure the nuclear interaction being smaller than 0.1% a separation of the nuclear surfaces of 5 fm is needed. This leads to D_{\min} being

$$D_{\min} \geq R_p + R_t + 5, \quad (3.3)$$

and is called Cline's criterion [Cli69].

For a classical description of the trajectory of the scattering nucleus the wave length λ of the projectile must be much smaller than the impact parameter $b(\Theta)$. This condition is described via the Sommerfeld parameter η

$$\eta = \frac{b(\Theta)}{2\lambda} = \frac{Z_p Z_t e^2}{\hbar v} \gg 1, \quad (3.4)$$

with v being the relative velocity of the two scattering partners. If this is fulfilled the trajectory of the incoming particle can be described by the well defined Rutherford scattering trajectory. In figure 3.1 this classical trajectory of a projectile nucleus A_p scattered at the Coulomb field of a target nucleus A_t is depicted. The differential cross section is given by the Rutherford formula

$$\left(\frac{d\sigma}{d\Omega} \right)_{\text{Rutherford}} = \frac{a^2}{\sin^4(\theta_{cm}/2)}, \quad (3.5)$$

with

$$a = \frac{e^2 Z_1 Z_2}{8\pi\epsilon_0 E}, \quad (3.6)$$

and Z_i being the proton numbers of the projectile and target, e is the electric charge, ϵ_0 is the dielectricity constant, E is the energy of the incoming particle and θ_{cm} is the scattering angle in the center of mass frame [Ald56, Ber07]. If the energy loss of the projectile in the target material is small compared to the beam energy, the assumption that the trajectory of the beam particle has not changed after excitation holds. Then the differential excitation cross section is directly related to the Rutherford cross section

$$\left(\frac{d\sigma}{d\Omega}\right)_{\text{exc}} = P_{if} \left(\frac{d\sigma}{d\Omega}\right)_{\text{Rutherford}}, \quad (3.7)$$

where P_{if} is the probability of an excitation from an initial state $|i\rangle$ to a final state $|f\rangle$. This probability can be written as the square of the absolute value of the transition amplitude a_{if} between these states

$$P_{ij} = |a_{if}|^2 \ll 1. \quad (3.8)$$

To calculate these amplitudes a quantum-mechanical approach is necessary by solving the time-dependent Schrödinger equation

$$i\hbar \frac{\partial}{\partial t} |\Psi(t)\rangle = H |\Psi(t)\rangle = (H_0 + V(\vec{r}(t))) |\Psi(t)\rangle, \quad (3.9)$$

with H_0 being the Hamiltonian of the non-interacting nucleus and $V(\vec{r}(t))$ the time-dependent electromagnetic interaction for one-particle excitation. The probability to mutually excite both particles is very small and is therefore neglected in the following considerations. Equation 3.9 can be solved using the eigenfunctions

$$|\Psi(t)\rangle = \sum_n a_n(t) |n\rangle \exp\left[-\frac{i}{\hbar} E_n t\right], \quad (3.10)$$

for eigenstates $|n\rangle$. The solution of equation 3.9 leads to a set of coupled differential equations

$$i\hbar \dot{a}_n(t) = \sum_m \langle n|V(\vec{r}(t))|m\rangle \exp\left[\frac{i}{\hbar} (E_n - E_m) t\right] a_m(t), \quad (3.11)$$

which can be solved using perturbation theory.

3.2 First order perturbation theory

3.2.1 First order effects

First order effects describe one-step excitations, which is the excitation of one state to another without any further excitations. In most of the experiments with light ions or low beam energy these are the only transitions that have to be considered.

For non-relativistic beam energies the main interaction $V(\vec{r}(t))$ in a collision is the Coulomb interaction. It is treated as a time-dependent perturbation of the system and can be expanded into a multipole series for electric excitation

$$V(\vec{r}(t)) = 4\pi Z_1 e \sum_{\lambda=1}^{\infty} \sum_{\mu=-\lambda}^{\lambda} \frac{1}{(2\lambda+1)r(t)^{\lambda+1}} Y_{\lambda\mu}(\theta(t), \phi(t)) \mathcal{M}(E\lambda, \mu), \quad (3.12)$$

with $Y_{\lambda\mu}(\theta(t), \phi(t))$ being the normalised spherical harmonics and $\mathcal{M}(E\lambda, \mu)$ the electric multipole moment of the nucleus defined as

$$\mathcal{M}(E\lambda, \mu) = \int \rho_E(\vec{r}(t)) r^\lambda Y_{\lambda\mu}(\theta(t), \phi(t)) d^3r, \quad (3.13)$$

with the spatial charge distribution $\rho_E(\vec{r}(t))$. Because of the multipole moments being tensor operators, the Wigner-Eckart-Theorem can be used. With this the full matrix elements can be rewritten as reduced matrix elements

$$\langle I_i M_i | \mathcal{M}(E\lambda, \mu) | I_f M_f \rangle = (-1)^{I_i - M_i} \begin{pmatrix} I_i & \lambda & I_f \\ -M_i & \mu & M_f \end{pmatrix} \langle I_i || \mathcal{M}(E\lambda) || I_f \rangle. \quad (3.14)$$

The advantage in using the reduced matrix element lies in the fact, that it is independent of the substate m and is therefore the same for any transition from a particular initial state i to a final state f . The reduced matrix element itself is connected to the reduced transition strength

$$\begin{aligned} B(E\lambda, I_i \rightarrow I_f) &= \sum_{M_f \mu} \left| \langle I_i M_i | \mathcal{M}(E\lambda) | I_f M_f \rangle \right|^2 \\ &= \frac{1}{2I_i + 1} \left| \langle I_i || \mathcal{M}(E\lambda) || I_f \rangle \right|^2. \end{aligned} \quad (3.15)$$

The transition amplitude can be written with equation 3.11 as

$$a_{if} = \frac{1}{i\hbar} \int_{-\infty}^{\infty} \langle f | V(\vec{r}(t)) | i \rangle \exp \left[i \frac{E_f - E_i}{\hbar} t \right] dt, \quad (3.16)$$

where the square of the absolute value $|a_{if}|^2$ is known as Fermi's golden rule. Inserting equations 3.5, 3.8 and 3.16 into equation 3.7 leads to the differential Coulomb excitation cross section for a one-step excitation

$$\frac{d\sigma_{E\lambda}}{d\Omega} = \left(\frac{8\pi^2 \epsilon_0 Z_1 e a}{\hbar} \right)^2 \frac{B(E\lambda)}{\sin^4(\theta/2)} \sum_{\mu} |S_{E\lambda,\mu}|^2, \quad (3.17)$$

with $S_{E\lambda,\mu}$ representing the orbital integral

$$S_{E\lambda,\mu} = \int_{-\infty}^{\infty} e^{i \frac{E_f - E_i}{\hbar} t} \frac{1}{r(t)^{\lambda+1}} Y_{\lambda\mu}(\theta(t), \phi(t)) dt. \quad (3.18)$$

The total differential Coulomb excitation cross section is given by the sum over all multipoles λ . As is seen above, the matrix elements involved in the excitation of a nucleon are the same as for the radiative transition of the same multipolarity. For an excitation the same selection rules as for a deexcitation apply

$$\left. \begin{aligned} |I_i - I_f| \leq \lambda \leq I_i + I_f, \\ \pi_i \cdot \pi_f = (-1)^\lambda, \end{aligned} \right\} \text{ for electric transitions} \quad (3.19)$$

with π representing the parity of a given state. But note that the transition strength for decay and excitation differs by a value depending on the spin of the involved states

$$B(\lambda, I_f \rightarrow I_i) = \frac{2I_i + 1}{2I_f + 1} B(\lambda, I_i \rightarrow I_f). \quad (3.20)$$

For the classification of a transition upon its strength it is convenient to express the transition strength in units of single particle excitations. Therefore V.F. Weisskopf introduced a "single particle unit" based on the shell model [Bla52], the *Weisskopf unit*, defined through

$$B_{W.u.}(E\lambda) = \frac{e^2}{4\pi} \left(\frac{3}{3 + \lambda} \right)^2 (1.2 \cdot A^{1/3})^{2\lambda} e^2 f m^{2\lambda}. \quad (3.21)$$

The calculations to obtain the cross section for magnetic excitations are similar to the ones outlined above. However, these transitions have very small cross sections for low energy Coulomb excitation and will therefore not be treated in this work. For a detailed description follow [Ald56].

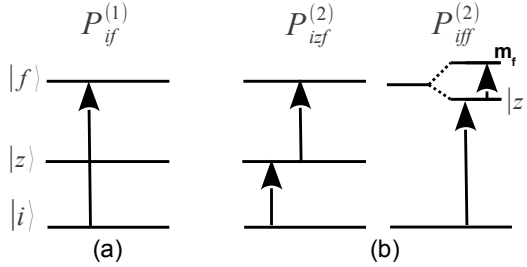


Figure 3.2.: Illustration of the excitation mechanisms of first (a) and second order effects (b). As a special case of $P_{izf}^{(2)}$, $P_{iff}^{(2)}$ represents the reorientation effect.

3.2.2 Second order effects

Second order effects describe two-step excitations and are therefore indispensable to consider when multi-step Coulomb excitations take place in the experiment. These multistep excitations occur for nuclei with more than one low-lying excited state and if the Coulomb interaction ($V(\vec{r}(t))$) (equ. 3.9) is large, that is for medium and relativistic beam energies. Furthermore they are necessary to include in the calculations for the extraction of the static nuclear quadrupole moment of the included states with $J \neq 0$.

For the formulation of second order effects an intermediate state $|z\rangle$ is introduced. The transition amplitude is the sum of the amplitudes of first and second order effects

$$a_{if} = a_{if}^{(1)} + \sum_z a_{izf}^{(2)}, \quad (3.22)$$

with

$$a_{izf}^{(2)} = \frac{1}{i\hbar} \int_{-\infty}^{\infty} \int_{-\infty}^{\infty} dt dt' \langle f | V(t) | z \rangle \exp \left[i \frac{E_f - E_z}{\hbar} t \right] \langle z | V(t') | i \rangle \exp \left[i \frac{E_z - E_i}{\hbar} t' \right], \quad (3.23)$$

and the first order term $a_{if}^{(1)}$ given via equation 3.16. The excitation probability includes first and second order effects as well as their interference

$$\begin{aligned}
 P_{if} &= \left| a_{if}^{(1)} + \sum_z a_{izf}^{(2)} \right|^2 \\
 &= \left| a_{if}^{(1)} \right|^2 + \left| \sum_z a_{izf}^{(2)} \right|^2 + 2\Re \left(\sum_z a_{if}^{(1)} a_{izf}^{(2)*} \right). \quad (3.24)
 \end{aligned}$$

A visualisation can be found in figure 3.2. For this work the most interesting second order term is $P_{iff}^{(2)}$ describing the reorientation effect. This is the reorientation of the nuclear axis of the beam particle after an excitation and is caused by the electric field of the scattering partner [Bre56]. The intermediate state $|z\rangle$ for this process is identical to one of the magnetic substates of the final level. It can therefore be understood as a change of distribution of the population of the magnetic substates. The reduced matrix element for this transition assuming an E2 character is connected to the spectroscopic quadrupole moment (Q_s) via the formula

$$eQ_s(I) = \sqrt{\frac{16\pi}{5(2I+1)}} \langle II20|I \rangle \langle I || \mathcal{M}(E2) || I \rangle. \quad (3.25)$$

with I being the spin of the final state $|f\rangle$ and $\langle II20|I \rangle = \langle j_1 m_1 j_2 m_2 | JM \rangle$ being the Clebsch-Gordon coefficient [Boh53]. Note that the reorientation effect is linear in Q . Therefore the sign of the quadrupole moment can be gained from a Coulomb excitation experiment through the matrix element. This sign tells about the type of deformation - whether the nucleus is prolate or oblate deformed.

3.3 Computation of Coulomb excitation cross sections - the CLX/DCY code

CLX and DCY are two computer programs written by H. Ower, adapted and modified by J. Gerl, Th. Kröll and K. Vetter, which together are able to calculate excitation probabilities and cross sections. For CLX input information on the mass and proton numbers of the projectile and target nucleus are needed as well as the projectile energy at the interaction point. As the exact place of scattering can not be determined from the experiment, the beam energy at half the thickness of the target is taken as an average. Further input are the information on the levels of the excited nucleus (energy, spin, parity) as well as the possible transitions between all included levels and their strength. CLX then creates an output containing all the statistical tensors, *i.e.* the occupation probabilities for the m substates, which are

needed in DCY. Together with this output information further input on the angles of the γ -detectors and the limiting angles of the particle detector in the center of mass frame is provided for DCY. Then the cross sections for the scattering experiment are calculated. The cross section of an excitation in a Coulomb excitation experiment strongly depends on the scattering angle of the involved nuclei. For a comparison of the theoretical output and the experimental cross section it is therefore crucial to cover the same angular ranges for the particle and γ -ray detection in the calculation and the performed experiment. By the variation of the input matrix elements the experimental cross section can be reproduced. The procedure of this variational process is discussed in detail in section 6.2.

4 The REX-ISOLDE facility and MINIBALL

The ISOLDE (Isotope Separation On Line DEvice) facility at the European Organisation for Nuclear Research, CERN, is one of the best choices for the investigation of exotic radioactive ion beams. In August 2011, when the experiment IS477 [Krö07] discussed here took place, this facility was the only one being able to produce a beam of ^{128}Cd in sufficient amount to perform a Coulomb excitation experiment in order to extract the transition strength $B(E2; 0_{gs}^+ \rightarrow 2_1^+)$ and the spectroscopic quadrupole moment $Q_s(2_1^+)$.

4.1 Beam production and extraction

At the ISOLDE facility the Isotope Separation On-Line (ISOL) technique is used to produce a radioactive ion beam [Lin04]. A thick primary target is bombarded with a 1.4 GeV proton beam and undergoes fission, spallation and fragmentation leading to a various amount of different products. The protons have an average intensity of $2 \mu\text{A}$ and are received from the Proton Synchrotron Booster (PSB) in bunches of $2.4 \mu\text{s}$ length. The time interval between two consecutive bunches is a multiple of 1.2 seconds. This time structure and the high intensity of the protons enhances the production of very short-lived radioactive isotopes like ^{128}Cd ($T_{1/2}(^{128}\text{Cd}) = 280 \text{ ms}$ (weighted mean from [Gok86] and [Mac86])) but has the disadvantage of highly stressing the target and its container, which can for example lead to leaks in the target container [Kug00]. There are more than 25 different target materials available, chosen to match the required production yield and beam purity. In the experiment discussed here a target made of UC_x - pellets was chosen, which was heated to temperatures above $2000 \text{ }^\circ\text{C}$. By heating the target the products diffuse through the porous material due to their chemical properties and are extracted via a transfer line into an ion source, which purifies the beam. At ISOLDE there are mainly three different types of ion sources available: a hot plasma, a hot surface and a laser ion source. For the production of a ^{128}Cd beam the combination of the UC_x - target and the Resonant Ionisation Laser Ion Source (RILIS) [Fed00] was found to provide the best chemical selectivity in order

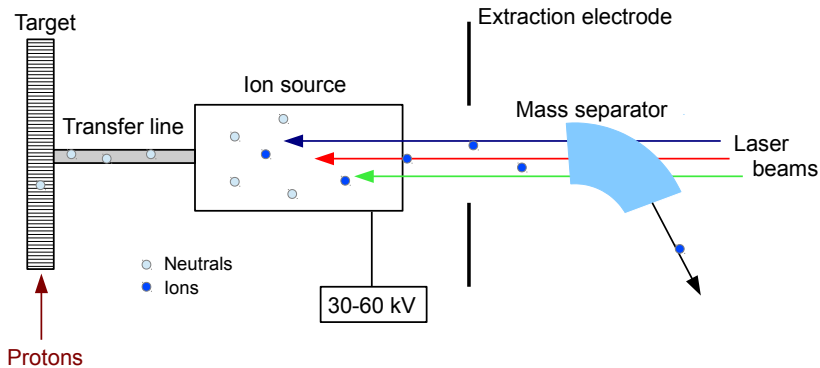


Figure 4.1.: Schematic view of the extraction process of the nuclei of interest at ISOLDE using a resonant laser ion source.

to extract a beam with sufficient yield. Figure 4.1 shows the extraction schematically. RILIS is a multistep laser system using the unique excitation scheme of an isotope for ionisation, which improves the selectivity tremendously compared to a single-step laser. In figure 4.2 the excitation scheme for the 3-step laser ionisation of ^{128}Cd is sketched. After ionisation the nuclei are extracted with 30-60 kV (30 kV for ^{128}Cd) into an electromagnet for a first mass separation. At ISOLDE two different mass separators are available: The General Purpose Separator (GPS) consisting of one bending magnet and a resolving power of ~ 1000 and the High Resolution Separator (HRS) with two bending magnets and a resolving power of ≥ 5000 [Kug00]. For the ^{128}Cd ions the HRS was used. A transmission rate of 80 % was gained.

4.2 Post acceleration

The isotopes produced with ISOLDE are accelerated further in order to investigate them. This is done via the Radioactive beam EXperiment (REX) [Kes03, Hab00], which consists of mainly three different parts: The REXTRAP for bunching and cooling of the ions, the REXEBIS for increasing the charge state and the REXLINAC for post-acceleration of the ions. The different components are depicted in figure 4.3 and will be explained in the following.

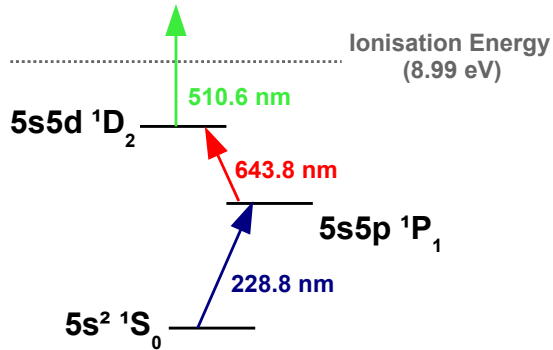


Figure 4.2.: 3-step excitation scheme of ^{128}Cd [Fed00].

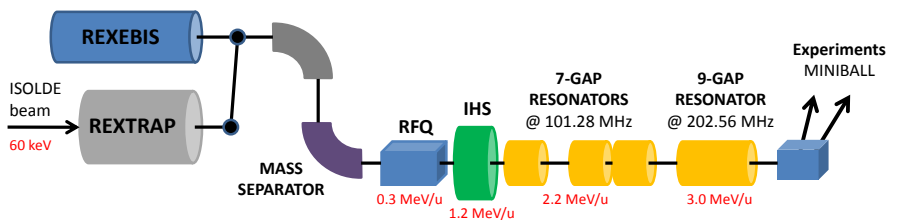


Figure 4.3.: Schematic view of the different components of REX.

REXTRAP

The REXTRAP is a 1 m long Penning Trap with a magnetic field of 3 T. At the entrance of the trap the ions need to pass a potential barrier in order to slow down. Collisions with an Argon or Neon buffer gas further decelerate the ions. A capture is possible if the energy loss of the ions in the trap in one oscillation is sufficiently large, such that they can not pass the potential barrier at the entrance again. This cooling down to a couple of eV increases the emittance of the beam. The accumulation and bunching increases the signal to background ratio for the measurements [Hab00] and is indispensable for the efficient injection into the REXEBIS. This process creates bunches of 100 ms length and usually takes a couple of ms.

REXEBS

The bunched and cooled ions are extracted into the Electron Beam Ion Source (EBIS). The ions are trapped by an electron beam in the radial direction and cylindrical electrodes with an applied potential in the longitudinal direction. By collisions with the electrons the ions undergo stepwise ionisation. An ultra-high vacuum is applied inside the EBIS in order to reduce the contamination from buffer gas from the REXTRAP. For the ^{128}Cd isotopes a charge state of 30^+ was achieved in a breeding time of 118 ms. The transmission of REXTRAP and REXEBIS was 3.3 %.

Mass separator

Although the amount of buffer gas ions is already reduced in the REXEBIS, its intensity is still larger or at least comparable to the intensity of the isotope of interest. Therefore further separation is of great importance and is realised with a second mass separation right after the charge breeding. However, as the ions are well spread in energy after the breeding, a simple magnet is insufficient. Therefore a more advanced spectrometer is used, which follows the idea of a Nier-spectrometer. Details of such spectrometers can be found in [Nie51]. The mass separation is possible for ratios of $A/q = 3 - 4.5$. For the ^{128}Cd isotopes a ratio of $A/q = 4.27$ was used.

REXLINAC

The purified beam is extracted into the LINear ACcelerator (LINAC), where the ions enter a 4-rod Radio Frequency Quadrupole (RFQ). It consists of four elec-

trodes focusing and accelerating the beam from 5 to 300 keV/u at a frequency of 101.28 MHz synchronised with the extraction from the REXEBIS. In the following Interdigital-H-type Structure (IHS) the beam is further accelerated up to 1.2 MeV/u. The three spiral 7-gap resonators, also operated at a frequency of 101.28 MHz, accelerate the ions to an energy of 2.2 MeV/u. Since 2004 this is followed by a 9-gap resonator used at 202.56 MeV where a final acceleration up to 3.0 MeV/u is possible. Eventually the beam is delivered to the experimental station. In the experiment discussed here the beam was accelerated up to 2.82 MeV/u. The transmission for the LINAC was 75 % which leads to an overall transmission of 2 % for the accelerated ^{128}Cd beam.

In figure 4.4 the special time structure of REX-ISOLDE is depicted [Gaf12].

4.3 Experimental area - MINIBALL

The purified and accelerated beam is delivered to the experimental area containing the MINIBALL detector array. Different kinds of experiments like transfer reactions and Coulomb excitation can be performed. In this work the latter has been used for the investigation of ^{128}Cd . For a Coulomb excitation experiment a special target chamber is mounted. It contains the secondary target placed on a target wheel with six positions, where the Coulomb excitation of the projectile and target nuclei takes place, and a Double-Sided Silicon Strip Detector (DSSSD) for the detection of the scattered particles. Surrounding the target chamber is the MINIBALL detector array to detect the γ -rays from the deexcitation of the Coulomb excited nuclei. As most of these states decay very fast, the γ -rays are emitted in flight, which leads to a Doppler shift of their energy. In order to correct for this, information about the angle between the emitting nucleus and the associated γ -ray plus the energy of the emitting nucleus need to be gained. This is achieved with the design of the DSSSD and the MINIBALL array and is discussed in the following.

4.3.1 Particle detection

The scattered particles are detected with a DSSSD (fig. 4.5) [Ost02], placed at a variable distance behind the target inside the target chamber. It consists of four individual silicon detectors, the quadrants, each segmented 16-fold in Θ (16 annular strips on the front side) and 12-fold in Φ (24 sector strips on the back side, each two paired together). The annular strips have a width of 1.9 mm and a 2 mm pitch, whereas the paired sector strips have a pitch of 6.8° . The gap between two quadrants is 8.4° . In the middle of the detector a hole with a radius of 9 mm

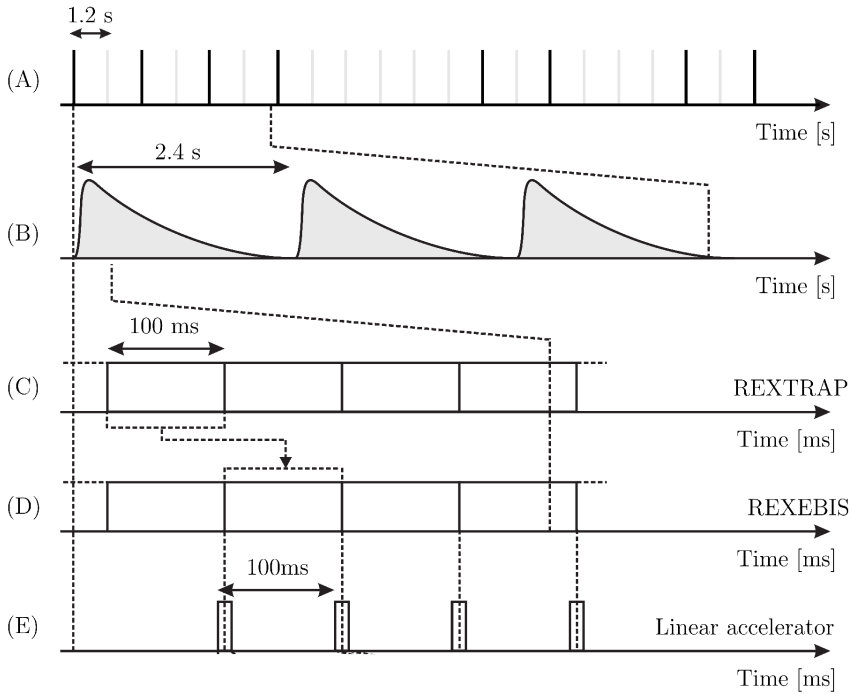


Figure 4.4.: Sketch of the timing structure at REX-ISOLDE. A) Proton bunches from the PSB with a width of $100 \mu\text{s}$ and a maximum frequency of 1.2 s. B) Possible release profile of an isotope from the primary target. Note, that this looks differently for every isotope and target material depending on the chemical properties, amount of surface ionisation and lifetime of the nucleus of interest. C) Bunches of the REXTRAP. D) Bunches of the REXEBIS. E) Window of the radio frequency of the REXLINAC synchronised with REXTRAP and REXEBIS. This is dependent on the breeding time [Gaf12].

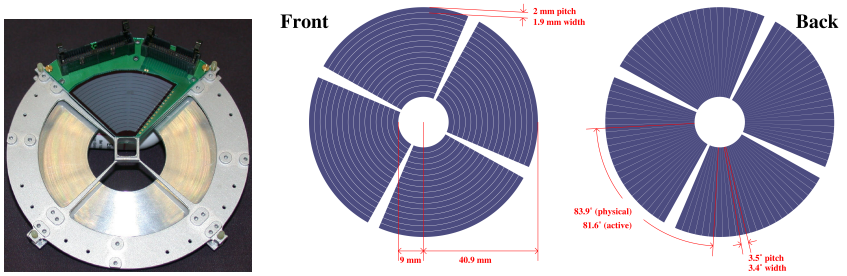


Figure 4.5.: Left: Picture of the front side of the DSSSD. Only the uppermost quadrant is mounted. Taken from [War13]. Right: Dimensions on the front and back side of the DSSSD. Taken from [War14].

can be found. The entire DSSSD has a radius of 42.5 mm. In this experiment the detector was placed at a distance of 32.2 mm from the target covering a laboratory scattering angle of $\Theta_{\text{Lab}} \simeq 15.6^\circ - 51.8^\circ$. The particles scattered at a small laboratory angle ($\Theta_{\text{Lab}} < 15.6^\circ$) and the non-scattered particles fly through the hole in the middle of the DSSSD and are collected either in a beam dump, where the beam is stopped, or in a $\Delta E - E$ telescope (fig. 4.6). In the $\Delta E - E$ telescope the energy loss ΔE is measured in a ~ 2.2 cm thick CF_4 -gas volume. The rest energy E_{rest} of the nuclei is detected with a silicon detector. As the energy loss is proportional to the proton number Z , this device can be used for particle identification. Note, that the telescope can only be used without a secondary target.

4.3.2 γ -ray detection

The deexcitation γ -rays are detected with the High-Purity Germanium (HPGe) detector array MINIBALL (fig. 4.7) [War13], which is especially designed for experiments with low-intensity RIBs and low multiplicity. It consists of eight triple cluster detectors each six-fold electronically segmented. Besides the signals from each segment also the signals from the core are written out (fig. 4.8). The high granularity is needed to account together with the information on the emitting nuclei for the Doppler shift correction of the energy of the γ -rays (see section 5.2.4). MINIBALL covers $\sim 60\%$ of the full solid angle. The detectors are placed on arms movable in directions θ and ϕ around the target chamber for optimal placement according to the experimental requirements. The efficiency at 1.3 MeV is 7 %. The signals are read out with digital electronics in a triggerless mode.

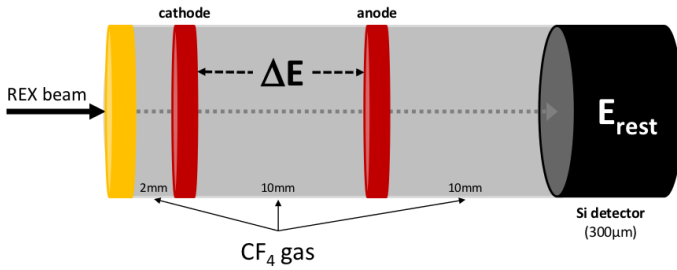


Figure 4.6.: Sketch of the $\Delta E - E$ telescope used for particle identification.

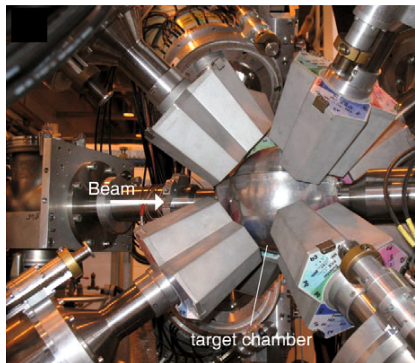


Figure 4.7.: Picture of a part of the Miniball detector surrounding the target chamber. Taken from [War13].

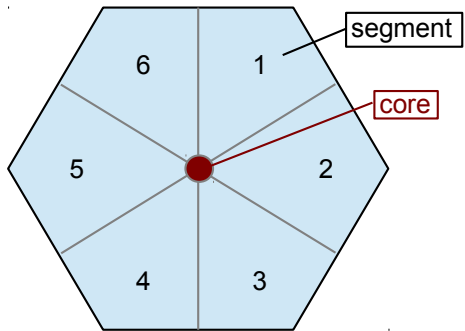


Figure 4.8.: Sketch of one 6-fold segmented HPGe cluster detector of MINIBALL.



5 Experimental details

The success of the analysis of a Coulomb excitation experiment highly depends on the precise knowledge of the experimental setup and conditions. In the following chapter, details on the delivered beam and chosen target as well as the experimental setup are discussed.

5.1 Beam and target details

The radioactive ion beam was delivered to the target chamber with an energy of 2.82 MeV/u and an average intensity of $\sim 3 \cdot 10^3$ pps. The choice of the secondary target is based on different considerations. First of all the target element needs to be stable and the aggregation state at room temperature needs to be solid in order to form a thin foil. In our analysis the Coulomb excitation cross section of the projectile is normalised to the target excitation in order to reduce systematic errors from target thickness, efficiency correction etc. . Therefore a sufficiently large cross section for the target (and projectile) excitation is indispensable. Additionally, the excitation energies of projectile and target need to be sufficiently different in order to distinguish the peaks in the γ -ray spectrum. The kinematics of the scattered target and projectile particles need to be such that they can be detected on the DSSSD and are furthermore as well distinguishable. To fulfil all of these conditions usually leaves the experimentator with only very few choices. For the Coulomb excitation experiment of low-energetic ^{128}Cd a target of ^{64}Zn was found to be the most convenient fulfilling the constraints mentioned above. The beam energy of 361 MeV is considered “safe” due to the fulfillment of the requirements considered in chapter 3.1. Figure 5.1 shows clearly, that the distance of closest approach D_{\min} for a “safe” scattering experiment is below the actual distance of the nuclei for every possible center of mass scattering angle. The first excited 2^+ -state of ^{128}Cd was expected at an energy of 646 keV [Kau00, Lea09] whereas for ^{64}Zn it is located at 992 keV, which is sufficiently different. In figure 5.2 the cross section for the transition $0_{\text{gs}}^+ \rightarrow 2_1^+$ in ^{64}Zn and ^{128}Cd is shown calculated with CLX/DCY for the experimental conditions in steps of 5° in Θ_{cm} . For ^{128}Cd the matrix elements $M_{02} = 0.4$ eb and $M_{22} = 0$ eb are assumed. The summed cross section for the range of the particle detection is 0.59 b for ^{64}Zn and 0.53 b for ^{128}Cd . Note the non-symmetric dependence of the Coulomb excitation cross section on

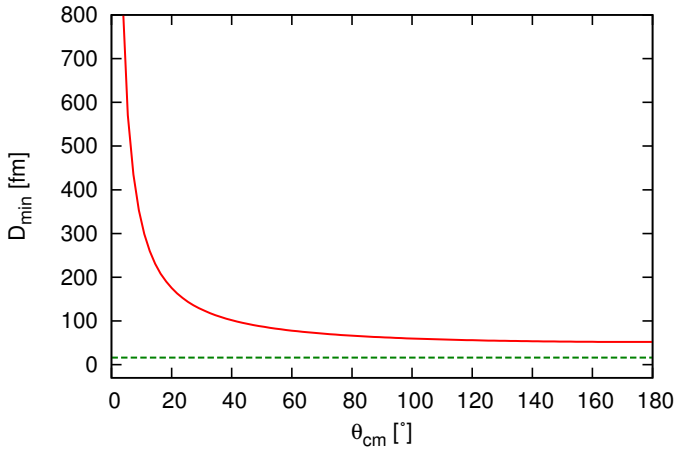


Figure 5.1.: Distance of closest approach D_{min} for ^{128}Cd nuclei scattered at ^{64}Zn with respect to the center of mass scattering angle Θ_{cm} . The dashed green line shows the limit for a “safe” scattering experiment according to equ. 3.3. The solid red line depicts the actual distance between the nuclei for the used beam energy of 2.82 MeV/u according to equ. 3.2. The requirements for “safe” Coulomb excitation are fulfilled in the performed experiment.

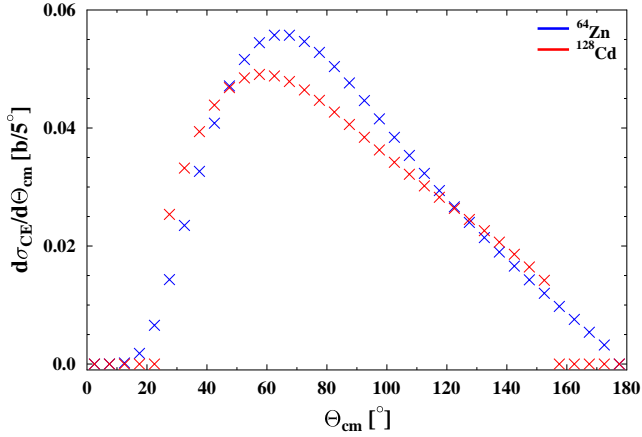


Figure 5.2.: Coulomb excitation cross section for $0_{gs}^+ \rightarrow 2_1^+$ transition in ^{64}Zn (blue) and ^{128}Cd (red) for the scattering process $^{64}\text{Zn}(^{128}\text{Cd}, ^{128}\text{Cd}^*)^{64}\text{Zn}^*$ calculated with CLX/DCY in Θ_{cm} steps of 5° . The matrixelements for ^{128}Cd were set to $M_{02} = 0.4$ eb and $M_{22} = 0$ eb. Other parameters taken as in the discussed experiment.

the scattering angle. The kinematics of the scattering process is shown in figure 5.3 with the range of the particle detector indicated with red lines. Note, that for the comparison to the experiment, the effect of the pulse height deficit has to be taken into account. This is the energy loss of the nuclei due to elastic scattering with the detector material. It is larger for heavier nuclei and will therefore shift the green line to lower energies. Therefore the projectile and target nuclei will be well distinguishable in the particle detector also for small laboratory scattering angles. The thickness of the target was 1.48 mg/cm^2 .

5.2 Calibrations and corrections

Energy and efficiency calibration of the γ -detectors are indispensable for the analysis of the collected data. Furthermore, corrections for broken detectors etc. need to be performed as it affects the amount of detected γ -rays and particles. In this section the energy and efficiency calibration as well as the performed corrections including the correction for Doppler broadening of the γ -rays, are discussed.

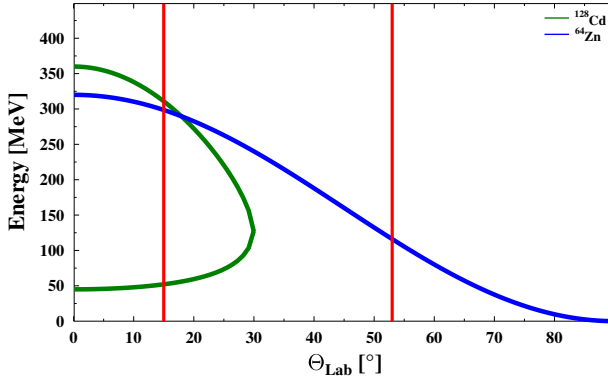


Figure 5.3.: Scattering kinematics of the experiment ${}^{64}\text{Zn}({}^{128}\text{Cd}, {}^{128}\text{Cd}^*){}^{64}\text{Zn}^*$ with a beam energy of 2.82 MeV/u. The scattered projectiles are indicated by the green line, the scattered target particles by the blue line. The red lines show the limits for the particle detection.

5.2.1 Energy and efficiency calibration

The energy and efficiency calibration of the HPGe detectors of the MINIBALL array were done with a measurement of a ${}^{152}\text{Eu}$ source placed at target position. The source ${}^{152}\text{Eu}$ was chosen since the emitted γ -rays have energies between 121.8 keV and 1408 keV, which is exactly the range needed for the experimental purpose. At the time of the measurement the activity was 6.2 kBq and the measurement took place for one hour. The function for the energy calibration is linear in energy E , whereas the function for the efficiency ϵ of a germanium detector is highly non-linear. A fit to the data points $\epsilon \equiv \frac{N_\gamma}{I_\gamma}$ with N_γ being the γ -ray yield in the photopeak and I_γ its relative intensity, requires a polynomial function on a logarithmic scale. Here, a function with four parameters is chosen to fit the data points:

$$f(E) = \exp \left[a + b \ln(E) + c \ln^2(E) + d \ln^3(E) \right]. \quad (5.1)$$

A characteristic of the MINIBALL detectors in this experiment is that no anti-Compton shields were used in order to increase the efficiency. Therefore it is possible that a Compton scattered γ -ray is detected in two neighbouring cores each with a fraction of its total energy. This is corrected with the so-called add-back routine. If two γ -events are detected within 100 ns in neighbouring cores on

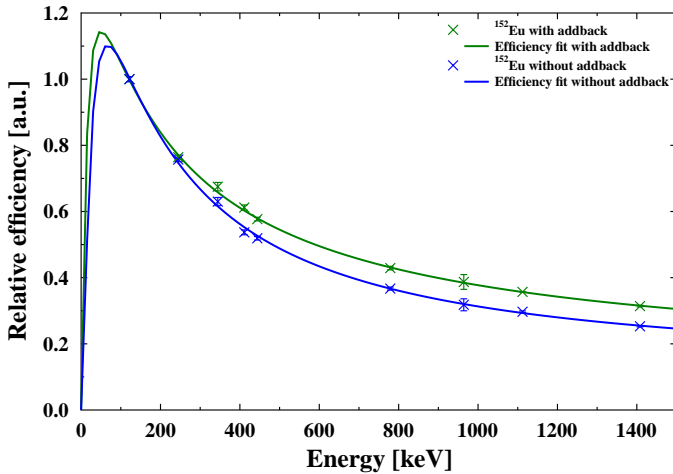


Figure 5.4.: Relative efficiency of the MINIBALL detector array determined with a ^{152}Eu source and the fit function in equ. 5.1.

the same cluster it is assumed as being the same γ -ray, just Compton scattered, and the implanted energies are summed up. This procedure increases the efficiency for high-energy γ -rays because a Compton scattering is much more likely than for low-energetic ones. In figure 5.4 the efficiency curves with and without addback are shown. Note that at energies below 100 keV the efficiency of a germanium detector decreases dramatically. This can not be extrapolated from the data taken with the ^{152}Eu source. Since for this experiment only the energies above 120 keV are of interest, this effect does not have to be considered.

5.2.2 HPGe-detectors

It often happens during an experiment that not all of the detectors work properly, which might be possible to correct in the offline analysis. In particular for the germanium detectors at MINIBALL it is possible to correct for broken segments in a detector. If a segment is broken, no signal is read out when a γ -ray hits the detector material. Since not only the segment signals but also the signals of the core are read out, an event in a broken segment still gives a core signal (fig. 4.8).

In the case of one broken segment in a core, events detected without a segment id can be assigned by hand to a particular angle - the angle of the broken segment. If two or more segments are broken in the same detector, the angle of the core is assigned. The identification of the correct angle for a γ -ray event is crucial for the Doppler correction. In this experiment six out of 144 segments were broken, twice two of them in the same detector. In addition two complete detectors out of 24 were broken, so that 22 detectors operated during the experiment.

5.2.3 DSSSD

For the calculation of the cross section with CLX/DCY it is very important to know the angular coverage of the particle detector in the center of mass frame. Additionally to the four open areas between the quadrants and the 9 mm hole in the middle (fig. 4.5), two rings were broken where no particles could be detected. One of the broken rings was settled in quadrant number one, being the innermost one at $\Theta_{\text{Lab}} = 15.6^\circ - 18.9^\circ$, the other one was in quadrant number three, leaving a gap at $\Theta_{\text{Lab}} = 20.7^\circ - 23.9^\circ$ (see fig. 5.5). In order to account for the broken rings and the position of the gaps between two quadrants correctly, the rotation of the DSSSD in Φ has to be determined. This is most easily done by plotting the rotation against the Doppler corrected energy. The correct rotation is then determined by the value where the energy spread after Doppler correction is the smallest. In this experiment the rotation of the DSSSD was determined to be 215.5° .

Beam shift

In most of the experiments the beam is not perfectly centered as seen in figure 5.5 and therefore does not impinge in the middle of the secondary target. This has to be corrected as it affects the assigned scattering angle, which has further impact on the Doppler correction and the calculation of the cross section with CLX/DCY. The scattering process is symmetric in Φ and therefore all four quadrants have to detect the same amount of particles. For the angle Θ the scattering follows the Rutherford formula

$$N \propto \frac{1}{\sin^4(\Theta_{\text{cm}})}, \quad (5.2)$$

where N is the number of scattered particles and Θ_{cm} is the scattering angle in the center of mass frame. By comparing several distinct ranges of the center of mass scattering angle in the different quadrants, the beam position can be shifted such that the amount of scattered particles in each quadrant is comparable. Additionally

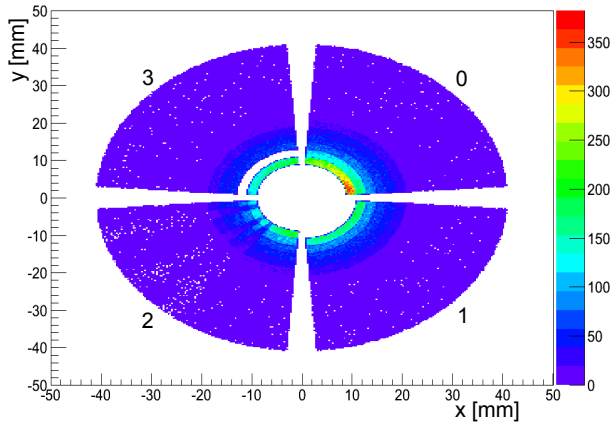


Figure 5.5.: Hits on the DSSSD from the discussed experiment. Two rings are missing and the beam is slightly off-center.

the turning point of the scattered projectile particles (see fig. 5.3) needs to be at the same angle for all of the quadrants. For ^{128}Cd on ^{64}Zn this turning point lies at $\sim 30^\circ$. The beam shift was determined to be 1 mm in x-direction and 1 mm in y-direction.

In Table 5.1 the angular coverage of the DSSSD is given.

Table 5.1.: Angular coverage of the particle detector.

Quadrant	$\Theta_{\text{Lab}} [^\circ]$	$\Phi [^\circ]$
0	$\sim 16.0 - 51.8$	$216.8 - 297.5$
1	$\sim 17.0 - 51.8$	$306.5 - 34.8$
2	$\sim 16.0 - 51.8$	$44.2 - 124.8$
3	$\sim 17.8 - 20.7$	$133.0 - 208.0$
3	$\sim 23.9 - 52.4$	$133.0 - 208.0$

5.2.4 Doppler correction

In order to account for the angle dependent Doppler shift of the energy E_0 of the emitted γ -rays, the angle ϑ between the emitting nucleus and the corresponding γ -ray as well as the detected γ -energy E_{Lab} in the laboratory frame need to be known. The correction factor is given by the Doppler shift according to the formula

$$\frac{E_0}{E_{\text{Lab}}} = \frac{1 - \beta \cos(\vartheta)}{\gamma}. \quad (5.3)$$

Here $\beta = v/c$ with v the velocity of the emitting particle and the relativistic factor $\gamma = 1/\sqrt{1 - \beta^2}$. The angle ϑ is calculated from the angles of the detected particle $(\Theta_{\text{part}}, \Phi_{\text{part}})$ and γ -ray $(\Theta_{\gamma}, \Phi_{\gamma})$

$$\cos(\vartheta) = \sin(\Theta_{\text{part}}) \sin(\Theta_{\gamma}) \cos(\Phi_{\text{part}} - \Phi_{\gamma}) + \cos(\Theta_{\text{part}}) \cos(\Theta_{\gamma}). \quad (5.4)$$

Rewriting β in terms of the energy of the emitting particle E_{part} as

$$\beta = \sqrt{\frac{2E_{\text{part}}}{A \cdot u}}, \quad (5.5)$$

the dependence of the Doppler shift on the mass A of the emitting particle and therefore the necessary kinematically separability is apparent. The energy of the emitting particle is calculated via the detected scattering angle on the DSSSD. The formulae and kinematical reconstruction of the scattering process can be found in more detail in Appendix A. With this information on the angles and the energy of the γ -ray from the Doppler corrected spectrum an event-by-event Doppler correction can be performed. Note that in the case of two coincident γ -rays in the same core, the one with the highest energy is assumed as being the first hit.

6 Data analysis

In a low-energy Coulomb excitation experiment of exotic beams, where the transitions of interest only have a small cross section and the particle yield is modest, it is indispensable to obtain the γ -ray spectrum as clean as possible. One technique to do so is to reduce the background by selecting only prompt particle- γ coincidences and subtracting the random ones. For this purpose a gate is set on the “prompt peak”, which means on short time differences (maximum 200 ns) between a hit on the DSSSD and a MINIBALL detector (see fig. 6.1). Note, that the prompt peak lies at -800 ns due to a delay of the signal from the DSSSD. Additionally, a downscaling has been applied, which reduces the number of random coincidences between a γ -ray from Bremsstrahlung, background radiation etc. and a particle. A hardware time window of 800 ns was set triggered by the detection of a γ -ray. From the coincidences outside of this window only 25 % are written to the data stream. This downscaling produces a plateau below the prompt peak. Therefore the random coincidence window is chosen four times larger than the prompt window for the subtraction.

To calculate the Coulomb excitation cross section for a projectile, different information is needed. With the beam purity \mathcal{P} , the γ -ray yield N_γ^{proj} for the transition of interest in the projectile and the normalising transition in the target nucleus, N_γ^{targ} , the corresponding efficiencies of the γ -ray detectors ε_γ at the energies for projectile and target excitation and the Coulomb excitation cross section for the target σ^{targ} , the Coulomb excitation cross section for the projectile σ^{proj} can be determined as

$$\sigma^{\text{proj}} = \frac{1}{\mathcal{P}} \frac{N_\gamma^{\text{proj}}}{\varepsilon_\gamma^{\text{proj}}} \left(\frac{N_\gamma^{\text{targ}}}{\varepsilon_\gamma^{\text{targ}}} \right)^{-1} \cdot \sigma^{\text{targ}}. \quad (6.1)$$

The quantity σ^{targ} is calculated via the matrix elements and the program CLX/DCY (see chapter 3.3). The energy loss of the beam in the target material is needed as an input parameter and calculated with the program SRIM [Zie04]. For ^{64}Zn only the 0^+ ground state and the first excited 2^+ state are involved in the excitation. Therefore only two reduced matrix elements are important: $M_{02} = \langle 0_{gs}^+ \parallel \mathcal{M}(E2) \parallel 2_1^+ \rangle$ and $M_{22} = \langle 2_1^+ \parallel \mathcal{M}(E2) \parallel 2_1^+ \rangle$ with $\mathcal{M}(E2)$ being the electric quadrupole operator. Contributions from higher lying

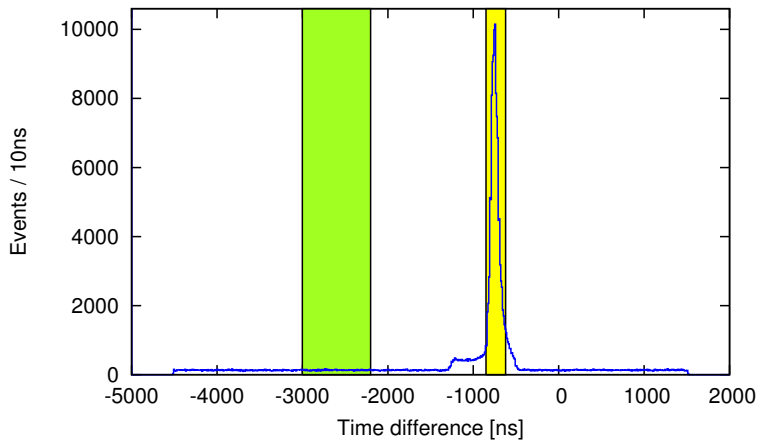


Figure 6.1.: Particle- γ coincidence spectrum. Prompt (yellow) and random coincidence window (green) are indicated. Due to downscaling a plateau arises below the prompt peak and the random time gate was chosen four times larger than the prompt gate.

states and electron conversion are negligible. For the calculation of σ^{targ} the values $M_{02} = 0.406(4)$ eb [Ram01] and $M_{22} = -0.0132_{-0.0660}^{+0.1188}$ eb [Ili14, Koi03] are used. Note that for the diagonal matrix elements two different values are found in literature [Koi03, Sal88]. Here, the value measured by Koizumi *et al.* [Koi03] is used due to elastic scattering comparison for a Coulomb excitation experiment of $^{122-126}\text{Cd}$ by Ilieva *et al.* [Ili14], which turned out to describe the data much better.

6.1 Beam purity

In equation 6.1 the influence of the beam composition is already apparent. The amount of contamination is important to know as the projectile cross section is normalised to the target cross section and all beam components interact with the target nuclei resulting in excitation. As a consequence, a different amount of detected γ -rays for the target excitation peak follows than expected for a pure beam. Most of the RIBs produced and delivered to a target are not 100 percent pure. In the case the ISOL technique is used this may be due to the extraction of surface ionised elements and/or to a short lifetime of the nucleus of interest, which results in decay products of this isotope to arrive at the experimental area. In the Coulomb excitation experiment discussed here different types of contamination were present in the beam. The identification and treatment will be discussed in the following.

6.1.1 Identification of contaminants

In figure 6.2 the energy loss ΔE versus the rest energy E_{rest} detected with the ΔE - E telescope (see chapter 4.3.1) is shown. Two areas at different energy loss are seen. The lower one at higher E_{rest} is identified as ^{128}Cd . As the resolution is not sufficient to resolve isotopes with only one proton difference, this area could also contain for example In and Sn isotopes, which are the decay products of Cd. These could indeed be identified as beam components via γ -spectroscopy after β -decay (see section 6.1.3) stemming from the decay of ^{128}Cd as well as directly from the beam production. As the energy loss is larger for isotopes containing more protons, the upper area at less E_{rest} stems from an isotope with more protons than $^{128}_{48}\text{Cd}$. It is identified as $^{128}_{55}\text{Cs}$. Having this contaminant in the beam is of no surprise as its ionisation potential is very low. Hence in the experiment discussed here we are dealing with two different types of contamination - one being a long living ^{128}Cs contamination ($T_{1/2}(^{128}\text{Cs}) = 3.6$ min [Alk93]) from surface ionisation, the other one being the daughter and granddaughter nuclei of the short living ^{128}Cd ($T_{1/2}(^{128}\text{Cd}) = 280$ ms [Gok86, Mac86]). In the following paragraphs the different treatments of these contaminants are discussed.

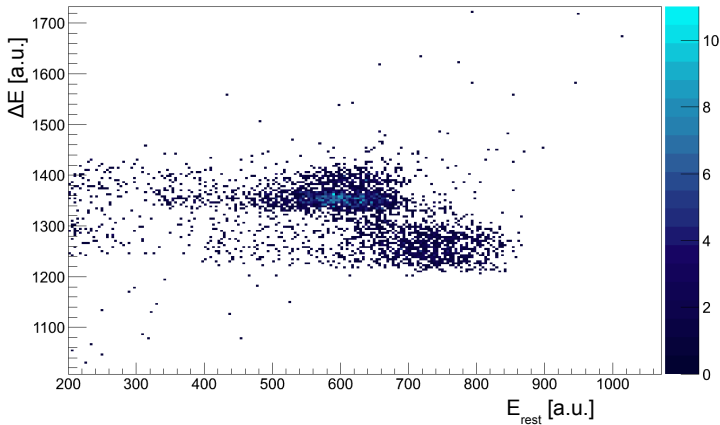


Figure 6.2.: Plot of the energy loss ΔE versus the rest energy E_{rest} detected with the ΔE -E telescope. Two areas with different energy loss can clearly be distinguished.

6.1.2 ^{128}Cs contamination

The ΔE -E telescope at the very end of the beamline reveals a high amount of ^{128}Cs (fig. 6.2) stemming from surface ionisation. Due to a little hole in the container of the primary target and the much higher volatility of ^{128}Cs compared to ^{128}Cd , the ratio $^{128}\text{Cs}/^{128}\text{Cd}$ got smaller with time as the hole got bigger (fig. 6.3). Due to low statistics in the Coulomb excitation peak of ^{128}Cd the relative amount of ^{128}Cs in the beam can not be known in detail throughout every minute of the experiment. However, the different half lives of this contaminant ($T_{1/2}(^{128}\text{Cs}) = 3.6$ min [Alk93]) and the nucleus of interest ($T_{1/2}(^{128}\text{Cd}) = 280$ ms [Gok86, Mac86]) plus the exclusive production of ^{128}Cs by surface ionisation and the special time structure at ISOLDE allow for an elimination of ^{128}Cs . As the protons hit the primary target in bunches with a frequency of $n \times 1.2$ s (with $n \geq 1$), gates can be set on early ($200 \text{ ms} \leq T \leq 1200 \text{ ms}$) and on late ($1300 \text{ ms} \leq T \leq 2300 \text{ ms}$) times T after proton pulse impact (fig. 6.4). Within the late time window the beam delivered to the secondary target does not contain any ^{128}Cd nuclei anymore as they are only produced right after the bombardment of the primary target. Note, that also in the first 230 ms after proton pulse impact no ^{128}Cd nuclei are delivered to the tar-

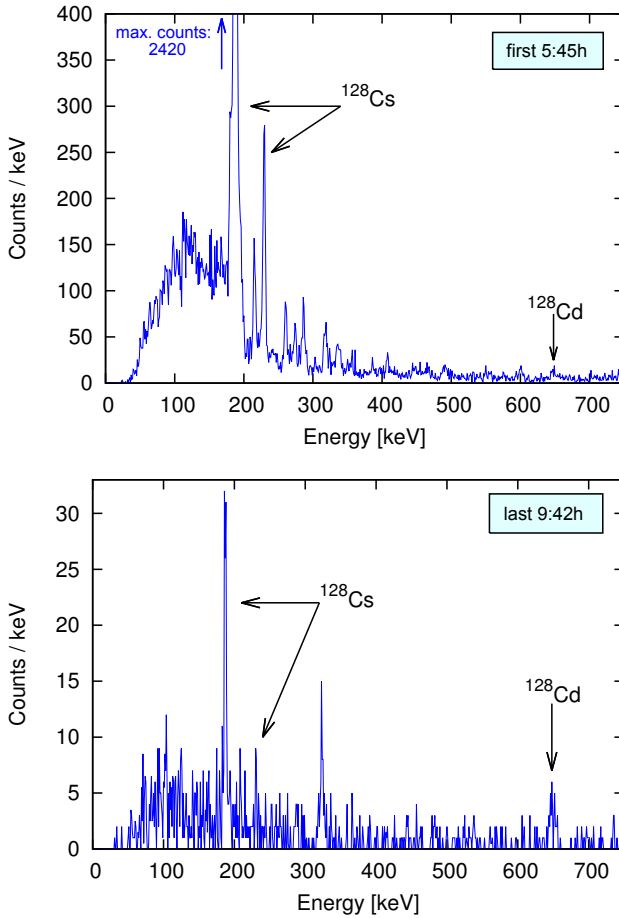


Figure 6.3.: Doppler corrected γ -spectra for the first 5:45h (top) and the last 9:42h (bottom) of the experiment. The ratio of the amount of $^{128}\text{Cs}/^{128}\text{Cd}$ changed by a factor of ~ 20 during the experiment.

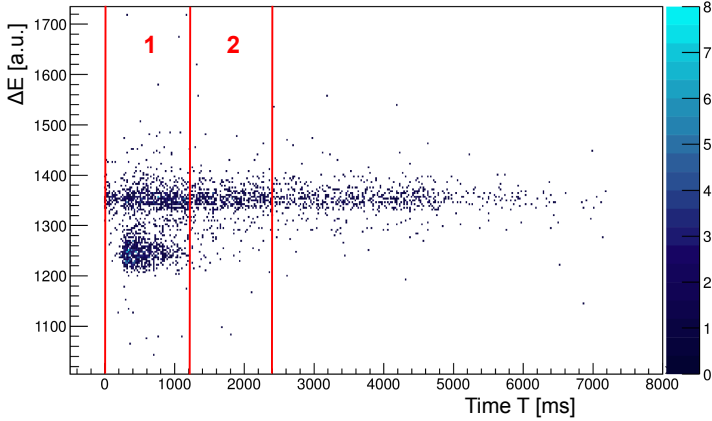


Figure 6.4.: Energy loss ΔE versus time T after proton pulse impact. Particles with higher energy loss correspond to ^{128}Cs , less energy loss to ^{128}Cd , ^{128}In , ^{128}Sn . The time gates (1: early, 2: late) are indicated.

get because of the extraction and acceleration process, whereas the surface ionised ^{128}Cs nuclei are transported continuously. By normalising those two gated γ -ray spectra to the strongest transition in ^{128}Cs (188 keV) and subtracting them from each other, any evidence of ^{128}Cs is removed.

6.1.3 ^{128}In and ^{128}Sn contamination

The time the ^{128}Cd nuclei need to propagate from the production to the secondary target (118 ms in the REXTRAP + 118 ms in the REXEBIS), is relatively large compared to its short half life ($T_{1/2}(^{128}\text{Cd}) = 280$ ms [Gok86, Mac86]). This causes an immense amount of decay products impinging on the secondary target. The decay product of ^{128}Cd is ^{128}In with $T_{1/2}(^{128}\text{In}) = 0.84$ s [Gok86], which further decays into ^{128}Sn with $T_{1/2}(^{128}\text{Sn}) = 59.97$ min [Kan01]. As the ΔE -E telescope is not capable to resolve nuclei with only one or two protons difference, the beam is stopped in a thick (14.89 mg/cm²) ^{64}Zn target throughout the experiment for a couple of minutes. The contaminants can then be identified by γ -spectroscopy after β -decay. Figure 6.5 shows the detected γ -ray spectrum. The beam com-

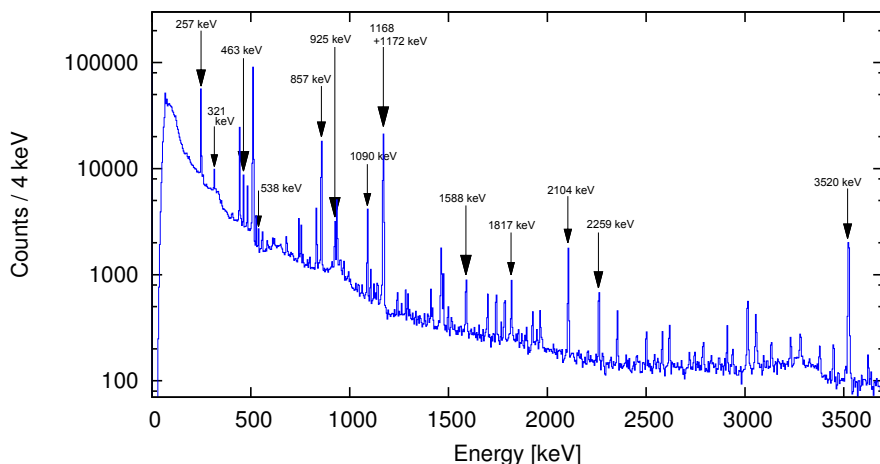


Figure 6.5.: γ -ray spectrum after β -decay of the beam implanted in a thick ^{64}Zn target with labeled transitions. Note that this spectrum is a sum spectrum over all available measurements with a thick target.

ponents identified by this method are ^{128}Cs , ^{128}In from ^{128}Cd decay and ISOLDE directly, $^{128\text{m}}\text{In}$ and ^{128}Sn from β -decay of ^{128}In and $^{128\text{m}}\text{In}$. Due to the long half life of ^{128}Sn its daughter nucleus ^{128}Sb is present in the beam only in a negligible amount. With the intensities of the transitions the relative amount of each component can be determined.

Determination of the γ -ray transition intensities

^{128}In

Information on the γ -ray intensities in ^{128}In only scarcely exist. Only in the proceedings by Fogelberg [Fog88] the level scheme including γ -ray intensities is discussed. Nevertheless, the relative γ -ray intensities can be determined from the decay of the ^{128}Cd nuclei implanted in the thick ^{64}Zn target. The relative intensities of the β -decay can not be determined as no appropriate transition for a comparison is present in the spectrum. Therefore these values have to be taken from [Fog88]. In figure 6.6 the level scheme of ^{128}In is depicted. Note that two transitions with an energy of 462.7 keV exist in this nucleus. Assuming the β -decay into the uppermost

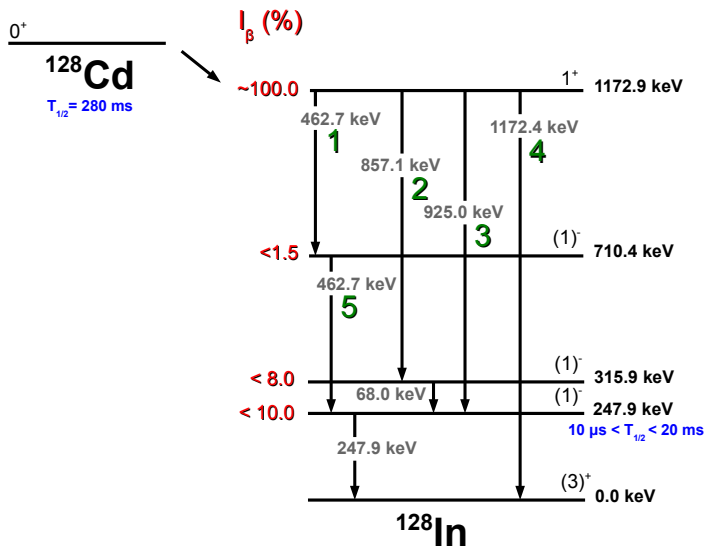


Figure 6.6.: Levelscheme of ^{128}In with β -intensities (red) and labeling of the transitions (green). Figure follows [Fog88].

Table 6.1.: Relative γ -ray intensities $I_{\gamma}^{\text{measured}}$ for ^{128}In with respect to a 100 % decay from the uppermost level at 1172.9 keV compared to the literature values [Fog88]. Numbering of the transitions as in figure 6.6.

Transition	Energy [keV]	$I_{\gamma}^{\text{measured}}$ [%]	$I_{\gamma}^{\text{Literature}}$ [%]
1	462.7	6.61(12)	6.9
2	857.1	73.17(31)	74.9
3	925.0	8.31(21)	9.8
4	1172.4	11.97(26)	10.8
5	462.7	6.61(12)	6.9

level at 1172.9 keV to be 100 % the amount of γ -rays corresponding to transition “1” ($N_{\gamma}^{(1)}$) and transition “5” ($N_{\gamma}^{(5)}$) are calculated via the formula

$$N_{\gamma}^{(1)} = \frac{N_{\gamma}^{(462.7 \text{ keV})}}{2} = N_{\gamma}^{(5)}. \quad (6.2)$$

The determined γ -ray intensities relative to the sum of decays from the uppermost level at 1172.9 keV are listed in table 6.1. The values from [Fog88] are given relative to the 247.9 keV transition and are converted for comparison. The error includes the statistical error and the error of the efficiency correction.

For two out of the seven lines it is not possible to determine the relative γ -ray intensity because of the following reasons: 1) The 68 keV line is too low in energy and no reliable value for the efficiency of the MINIBALL detectors exists. 2) The 248.9 keV transition is a transition from an isomeric state. The data are created with a 6 μs event window, which is the time between the beginning of an EBIS-pulse and a detected γ -ray. Only γ -rays within this time window are sorted in the spectrum. Therefore only transitions from levels with the same life time can be compared in order to obtain relative intensities.

^{128}Sn

By applying the same method as for ^{128}In , the relative intensities for the γ -ray transitions in ^{128}Sn are obtained. The level scheme of ^{128}Sn as well as the transitions in this nucleus and the corresponding probabilities have already been studied via the β -decay of ^{128}In by Fogelberg et al. [Fog79]. A speciality is, that there exists not only ^{128}In in the ground state but also an isomeric 8^{-} -state with $T_{1/2} (^{128m}\text{In}) = 0.72 \text{ s}$ [Gok86] decaying to ^{128}Sn . The ground and isomeric state populate identical as well as different levels and were both present in the beam.

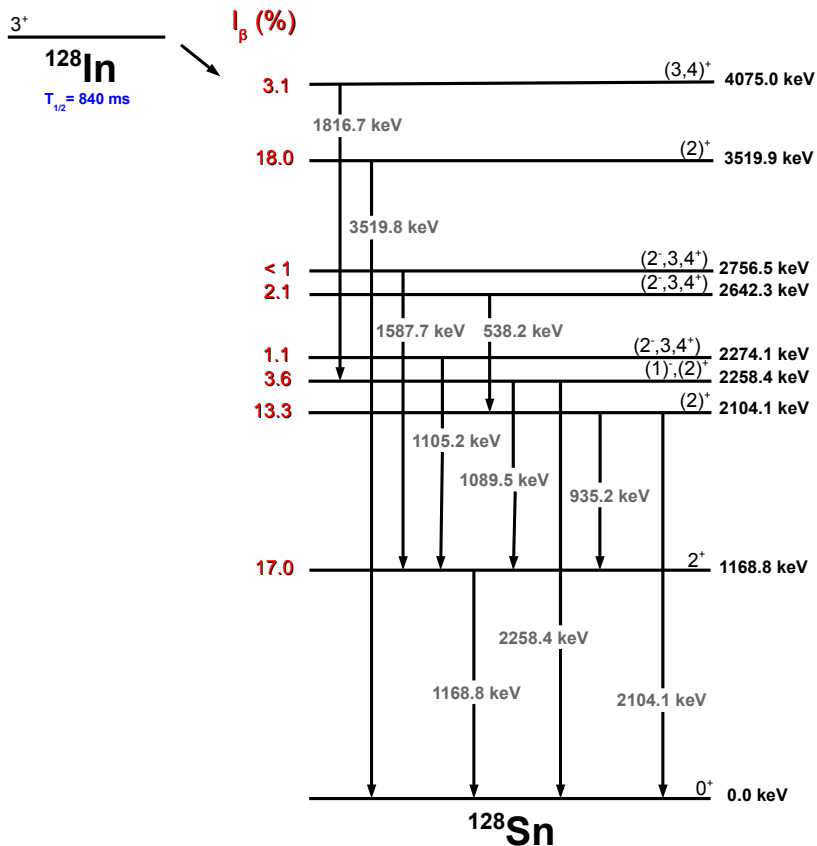


Figure 6.7.: Partial level scheme of ^{128}Sn after β -decay of ground state ^{128}In . Red: β -intensities. Figure follows [Fog79].

Table 6.2.: Obtained γ -ray intensities $I_{\gamma}^{\text{measured}}$ for ^{128}Sn after ground state ^{128}In decay relative to the total amount of decays compared to the literature values [Fog79].

Energy [keV]	$I_{\gamma}^{\text{measured}}$ [%]	Literature [%]
538.2	1.33(12)	1.20(8)
935.2	-	8.0(5)
1089.5	7.73(52)	7.4(5)
1105.2	1.37(12)	1.5(1)
1587.7	2.32(18)	2.4(2)
1816.7	1.96(16)	2.4(2)
2104.1	5.72(40)	6.5(4)
2258.5	2.73(20)	3.1(2)
3519.8	13.86(93)	16.6(15)

Figure 6.7 shows the partial level scheme of ^{128}Sn after the decay of ground state (gs) ^{128}In . For the determination of the relative amount of the different isotopes in the beam it is necessary to know the γ -ray intensities relative to 100 % of decays ($N_{\gamma}^{100\%}$) for each isotope. For the ground state decay of ^{128}In this is only possible by including a γ -ray intensity from [Fog79]. For this the 935 keV line was chosen as the transition clearly stems from the decay of the ground state ^{128}In and the error for the intensity is relatively small ($I_{\gamma} = 8.0(5)\%$). In table 6.2 the determined intensities for transitions in the ^{128}Sn nucleus after β -decay of the ground state ^{128}In relative to 100 % of decays are listed.

Figure 6.8 shows the partial level scheme of ^{128}Sn after the isomeric decay of ^{128m}In . The determination of the γ -ray intensities is more complicated than after the ground state decay. Low energetic transitions exhibit a non-negligible amount of electron conversion. The γ -ray yield $N_{\gamma}^{\text{transition}}$ of those has to be corrected for the amount of conversion and is given as

$$N_{\text{total}}^{\text{transition}} = N_{\gamma}^{\text{transition}} (1 + C^{\text{transition}}), \quad (6.3)$$

with the conversion coefficient $C^{\text{transition}}$. This situation applies especially to the transitions at 120.5 keV and 257.2 keV. Assuming the transitions having E1 and E2 character, respectively, the conversion coefficients are $C^{120.5 \text{ keV}} = 0.1070(15)$ and $C^{257.2 \text{ keV}} = 0.0590(9)$ [Kib08]. Another difficulty lies in the determination

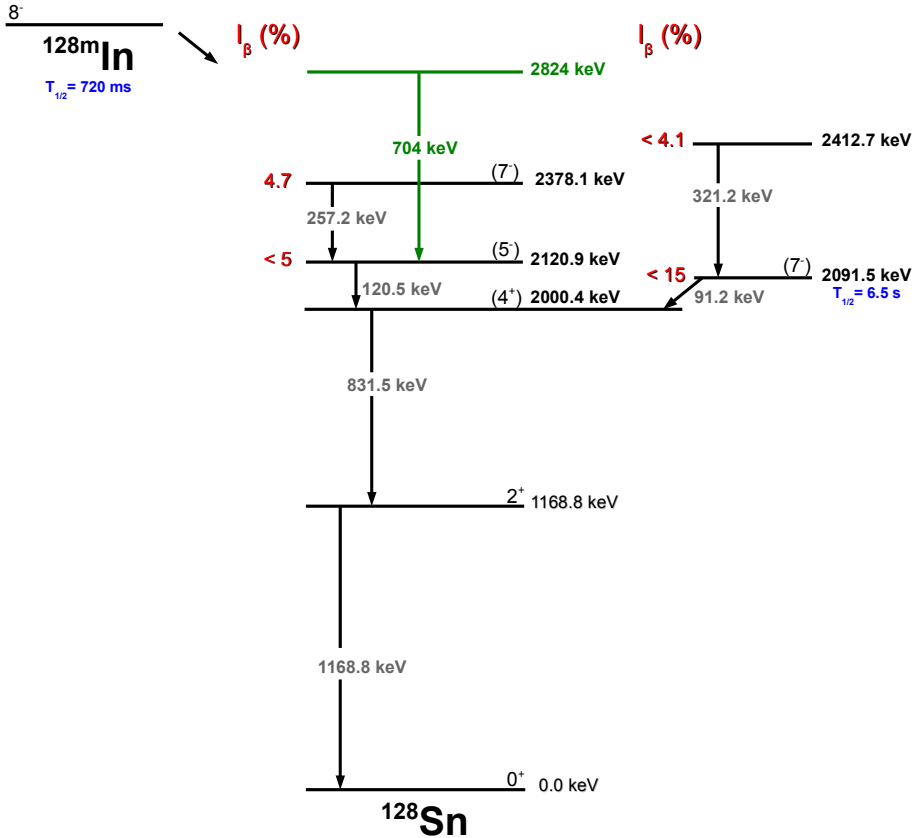


Figure 6.8.: Partial level scheme of ^{128}Sn after β -decay of isomeric ^{128m}In with β -intensities (red) following [Fog79]. Note the previously unknown level at 2824 keV with a transition of 704 keV to a lower level (green).

of the number of decays, which corresponds to 100 %. The determination of the total amount of decays via the 1168.8 keV transition is not possible, as it is also present after the β -decay of the ground state ^{128}In . Because all levels as well as the β -decay decay through the level at 2000.4 keV into the ground state (see fig. 6.8), the amount of ^{128m}In decays can be calculated via the amount of transitions with an energy of 831.5 keV. The γ -ray yield of the 831.5 keV transition is given as the sum of all feeding transitions $\left(N_{\gamma}^{100\%} = N_{\gamma}^{831.5\text{ keV}} = N_{\gamma}^{120.5\text{ keV}} + N_{\gamma}^{91.2\text{ keV}}\right)$. A decay via a γ -ray with 119 keV from a high spin state in ^{128m}In is reported [Pie11]. In order to undoubtedly assign the detected γ -rays in the peak around 120 keV to the transition from the 2120.9 keV level, $\gamma\gamma$ -coincidence spectra are used. Two spectra with a gate on the 831.5 keV transition and on the 1168.8 keV line are generated. The amount of counts in the 120.5 keV line is determined and corrected for electron conversion and detector efficiency. Note that for a $\gamma\gamma$ -coincidence spectrum the efficiencies of two lines, the gated transition and the transition of interest, have to be taken into account. The mean value out of these two calculations is taken to be the amount of deexcitation via the 120.5 keV line. The 91.2 keV transition is not usable from the γ -ray spectrum, as the efficiency of the MINIBALL detectors at this low energy is not known. Additionally the 2091.5 keV level has a half life of 6.5 s, which causes not all transitions via the 91.2 keV line resulting in a detected γ -ray with 831.5 keV or 1168.8 keV due to the 6 μs window already discussed for the ^{128}Cd decay. This fact has to be taken into account for further correction. Therefore the amount of actually detected relative to the expected γ -ray yield is simulated and a correction factor is determined. For the simulation it has to be taken into account, that the proton bunch hits the primary target only every couple of seconds and that therefore the EBIS transfers a beam only every couple of seconds. This has the consequence of a non-continuous feeding of the isomeric state. Additionally the electronics take data every new pulse of the EBIS, which is every 100 ms for the time of 1 ms (see fig. 4.4). In the case of the 6.5 s isomer in ^{128}Sn only 97.34 % of the expected γ -ray yield was detected in the time of the measurement due to the long level life time. The lifetime uncorrected amount of transitions via the 91.2 keV line can be calculated with the efficiency corrected γ -ray yields

$$N_{\gamma}^{91.2\text{ keV}} = N_{\gamma}^{831.5\text{ keV}} - N_{\gamma}^{120.5\text{ keV}}. \quad (6.4)$$

The 100 % mark is then set including the lifetime correction

$$100\% = N_{\gamma}^{120\text{keV}} + \frac{N_{\gamma}^{91.2\text{ keV}}}{0.9734}. \quad (6.5)$$

In the γ -ray spectrum (fig. 6.5) a transition at 704 keV can be noted. This transition is not sorted in the level scheme found by Fogelberg *et al.* [Fog79] due to an

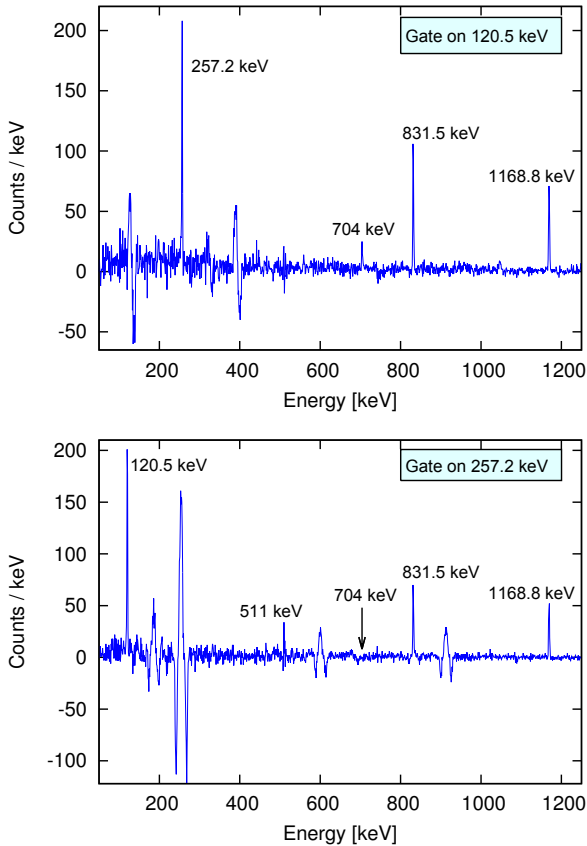


Figure 6.9.: Background subtracted $\gamma\gamma$ -coincidence spectra with a gate set on 120.5 keV (top) and 257.2 keV (bottom). A peak at 704 keV is clearly visible in the upper spectrum, but absent in the lower one. The peaks with a negative one on its side belong to Compton scattered γ -rays. If for example a γ -ray with 511 keV is Compton scattered in the detector material and implants an energy equal to the one where the gate is set, a coincident γ -ray is detected at the energy $511 \text{ keV} - E_{\text{gate}}$. The same applies for random coincidences, which produces the negative peaks when subtracted. Because the background was chosen to be on the left and the right hand side of the 257.2 keV gate, the negative peaks appear in two places for one energy.

Table 6.3.: Relative γ -ray intensities $I_{\gamma}^{\text{measured}}$ for ^{128}Sn from isomeric state ^{128}In decay compared to literature values [Fog79].

Energy [keV]	$I_{\gamma}^{\text{measured}}$ [%]	Literature [%]
120.5	48.49(270)	11.1(10)
257.2	29.36(167)	4.4(3)
321.2	12.15(161)	10.5(7)
704.0	6.35(134)	1.0(1)
831.5	100.0(293)	100.0(50)
1168.8	100.0(293)	100.0(50)

“unknown isomeric origin”. In our data clear coincidences could be evidenced. The $\gamma\gamma$ -coincidence spectrum in figure 6.9 (top) reveals coincidences of the 120.5 keV line with transitions of 257.2 keV, 704 keV, 831.5 keV and 1168.8 keV. The absence of a peak at 704 keV in the $\gamma\gamma$ -spectrum with a gate set on the 257.2 keV transition (fig. 6.9, bottom) leads to the placement of a previously unknown level at an energy of 2824 keV in the ^{128}Sn level scheme after the isomeric ^{128m}In decay (fig. 6.8).

In Table 6.3 the determined relative intensities are shown. In the Paper by Fogelberg *et al.* [Fog79] difficulties to obtain the amount of transitions following the decay of the 6.5 s isomeric state are reported. The large discrepancies between the here determined and the literature values are expected to stem from this difficulty.

Determination of the relative amount of isotopes in the beam

Due to different half lifes of the isotopes in the β -decay chain of ^{128}Cd , a different relative amount of detected decays to total decays is observed for each isotope. This is corrected in exactly the same way as the decay of the isomeric state discussed above. To determine the beam purity, a fit of the efficiency and the amount of each isotope to the intensity and lifetime corrected yields of ^{128}Cd and ground state ^{128}In was performed. Note that only transitions in the daughter nuclei with a higher intensity than 2.5 % and a smaller relative error of 2 % for transitions in ^{128}Sn (following the decay of ^{128}In) and 7 % for transitions in ^{128}In , respectively, are taken into account. The amount of ^{128m}In is included relatively to the ground

state ^{128}In determined via the total amount of decays. The relative amount \mathcal{P}^i of each isotope i is determined with the fit parameter f and the relations

$$\begin{aligned} f \cdot \mathcal{P}^{\text{Cd}} &= \mathcal{P}^{\text{Cd}} + \mathcal{P}^{\text{In}}, \\ \mathcal{P}^{\text{In}} &= x \cdot \mathcal{P}^{\text{In}_m}, \\ 1 &= \mathcal{P}^{\text{Cd}} + \mathcal{P}^{\text{In}} + \mathcal{P}^{\text{In}_m}, \end{aligned} \quad (6.6)$$

and is given as

$$\begin{aligned} \mathcal{P}^{\text{Cd}} &= 46.6_{-4.3}^{+4.5}\%, \\ \mathcal{P}^{\text{In}} &= 50.5_{-4.2}^{+4.0}\%, \\ \mathcal{P}^{\text{In}_m} &= 3.0_{-0.4}^{+0.5}\%. \end{aligned} \quad (6.7)$$

Recall, that the Cs contaminant is already subtracted.

6.2 Coulomb excitation analysis

In fig. 6.10 the prompt Doppler corrected, time and background subtracted γ -ray spectrum is shown. In contrast to figure 6.3 the low energetic part of the spectrum (below 300 keV) does not show any peaks from the excitation and decay of ^{128}Cs , yet only fluctuations are visible. The observation of a transition at 646 keV confirms unambiguously the previous assignment by Kautzsch *et al.* from β -decay studies of heavy Ag-isotopes [Kau00] and Cáceres *et al.* from data on isomeric ^{128m}Cd decay [Lea09] to be the $0_{gs}^+ \rightarrow 2_1^+$ transition in ^{128}Cd . The deexcitation of the first excited 2^+ -state of ^{64}Zn can be seen at 992 keV. Besides these two peaks a prompt transition at 324 keV is observed, which can only stem out of Coulomb excitation of the contaminant ^{128}In as the amount of ^{128m}In is not sufficient in order to produce the observed amount of γ -rays and no further contamination is present. Moreover, this transition has already been considered by Hellström *et al.* as being a transition in ^{128}In to the 3^+ ground state [Hel03]. However, as the deexciting level they propose an isomeric state with either $J^\pi = 1^-$ or 5^+ . The fact that this transition is seen prompt in the Coulomb excitation spectrum proofs the assignment as an isomeric state to be wrong. However, there could be an isomeric state present decaying with a low energy to the level at 324 keV. The low energy would not have been measured by Hellström *et al.*, but the 324 keV transition would still be delayed in the fission experiment [Hel03].

To achieve the main goal of a Coulomb excitation experiment, which is the extraction of the involved matrix elements, the experimental setup was designed in a

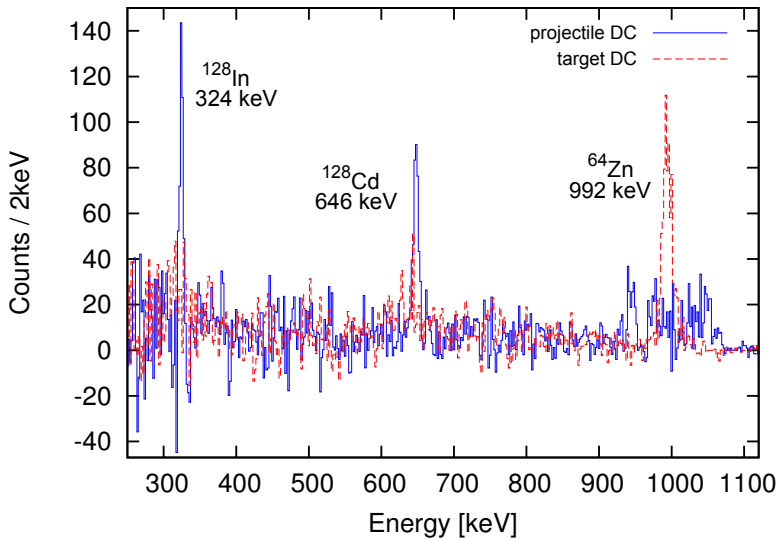


Figure 6.10.: Projectile (solid blue) and target (dashed red) Doppler corrected prompt γ -ray spectrum with indicated transitions in projectile and target nuclei. Note, that this spectrum is time and background subtracted and contains the full statistics.

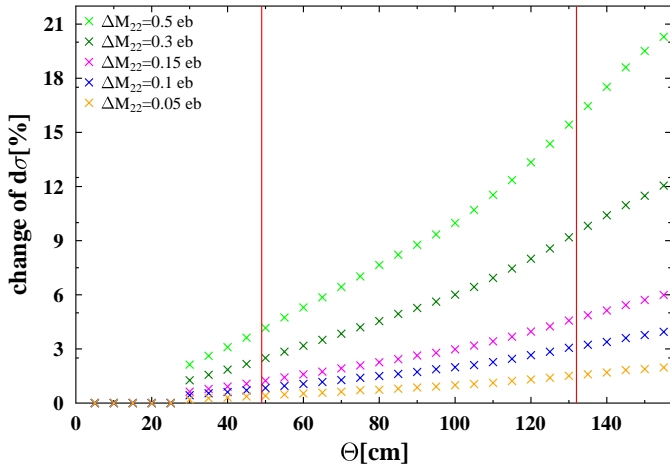


Figure 6.11.: Procentual change in the differential cross section for ^{128}Cd in the process $^{64}\text{Zn} \left(^{128}\text{Cd}, ^{128}\text{Cd}^* \right) ^{64}\text{Zn}^*$ with respect to $M_{22} = 0$ eb for different Θ_{cm} . The calculations are done in steps of 5° with the parameters from the experiment and $M_{02} = 0.4$ eb. The red lines indicate the angular range of the DSSSD in Θ_{cm} . The influence of M_{22} increases with Θ_{cm} .

way such that it is sensitive to the observables. In order to put a constraint on the diagonal matrix element, the particles need to be detected under different scattering angles as the influence of the diagonal matrix element on the differential cross section is not constant for different center of mass angles. Figure 6.11 shows the procentual change of the differential cross section of ^{128}Cd for the scattering process $^{64}\text{Zn} \left(^{128}\text{Cd}, ^{128}\text{Cd}^* \right) ^{64}\text{Zn}^*$ with respect to $M_{22} = 0$ eb over the center of mass scattering angle. The calculation is performed with CLX/DCY with the parameters from the experiment assuming $M_{02} = 0.4$ eb for ^{128}Cd and scattering angle windows of 5° . The procentual change increases with the scattering angle. Since the particle detector covered a continuous angular range, the scattered particles are divided during the offline analysis into distinct center of mass angular ranges. The Coulomb excitation cross section for the target and the projectile, respectively, are calculated with CLX/DCY and according to equation 6.1 for each experimental set, *i.e.* each angular range. To reproduce this experimentally found value for the projectile, a set of different combinations of transition (M_{ij}) and diagonal (M_{jj}) matrix elements is possible. Because the influence of the diagonal matrix element increases with increasing Θ_{cm} , bands with different slopes are obtained in the M_{ij} - M_{jj} -plane for the different angular ranges. To find the most likely combination of matrix elements, a maximum likelihood analysis is performed, see *e.g.* [Ber12]. Here the likelihood function \mathcal{L} is the product of the probability functions P for each set x_k of matrix elements, that is each angular range

$$\mathcal{L} = \prod_{k=1}^N P(x_k; M_{ij}, M_{jj}). \quad (6.8)$$

The probability functions are represented by a Gaussian shaped distribution function

$$P = \frac{1}{\sqrt{2\pi}\sigma} \exp \left[-\frac{(x - \mu)^2}{2\sigma^2} \right], \quad (6.9)$$

with the mean $\mu = M_{ij}$ and standard deviation $\sigma = \Delta M_{ij}$, where M_{ij} is a function of M_{jj} . The maximum value of \mathcal{L} is found by solving the equation

$$\frac{\partial \ln \mathcal{L}}{\partial M_{ij,jj}} = 0. \quad (6.10)$$

Because of the Gaussian shape of \mathcal{L} , the standard deviation σ of the estimators is given by

$$\ln(\mathcal{L} + s\sigma) = \ln \mathcal{L}_{max} - \frac{s^2}{2}, \quad (6.11)$$

with s being the order of the standard deviation.

6.2.1 Details on ^{128}Cd

The states involved in the Coulomb excitation of ^{128}Cd are the 0^+ ground state and the first excited 2^+ state. Therefore the matrix elements of interest are the M_{02} and M_{22} . To obtain decent values for those, a lot of different angular ranges and combinations of probability functions have been tested. It is of great importance to find the best likelihood function with respect to sufficient statistics and large enough difference in the slope of the M_{02} - M_{22} bands. Figure 6.12 shows the scattered particles on the DSSSD with three cuts as used for the analysis of ^{128}Cd . Note, that the region of the turning point in the projectile-like particle branch is excluded because of the rapid change of the center of mass scattering angle. For the three distinct angular ranges the efficiency corrected and background subtracted γ -ray yield for projectile and target excitation is given in Table 6.4. With this information the experimental Coulomb excitation cross section is calculated and reproduced with CLX/DCY for the different combinations of the involved matrix elements. The diagonal matrix element has been varied between -3 and 4.5 eb. In the calculation, statistical errors as well as errors from the beam purity, efficiency correction and of the target matrix elements are included. Figure 6.13 shows the bands obtained in the M_{02} - M_{22} -plane, where a large overlap can be noticed. The maximum likelihood analysis leads to the 1σ contour (fig. 6.14). The contour does not close for large positive M_{22} , which can be explained by looking at the bands in figure 6.13. The three bands together have a large overlap over almost the whole plotted range for M_{22} because of large errors and the limited sensitivity in these angular ranges (compare fig. 6.11). The most likely value for the transition matrix element is indicated in figure 6.14 with red lines showing the projections onto the axes. The error is marked by the red dashed lines. This analysis leads to $M_{02} = 0.42_{-0.11}^{+0.09}$ eb, where the lower limit is the value for a diagonal matrix element of 3 eb, which is already considered as an unphysical value. By excluding the intermediate angular range, *i.e.* cut 2, the intersection region of the bands is significantly reduced and the 1σ contour has a clear limit also at large positive diagonal matrix elements (fig. 6.15). The most likely value for the transition matrix element is then given as $M_{02} = 0.44_{-0.12}^{+0.10}$ eb. This is in perfect agreement with the analysis including three different angular ranges. However, the error is slightly larger due to the reduction of the statistics. Note the emergence of a second maximum at large positive M_{22} for both choices of cut combinations. This peculiarity has already been observed in Coulomb excitation experiments of Kr isotopes [Alb13], for example, and is an effect of the method. However, no problems arise from this second maximum as it lies at clearly unphysical values and does not have to be considered further. It is already seen from the 1σ contours, that the error for the extraction of the di-

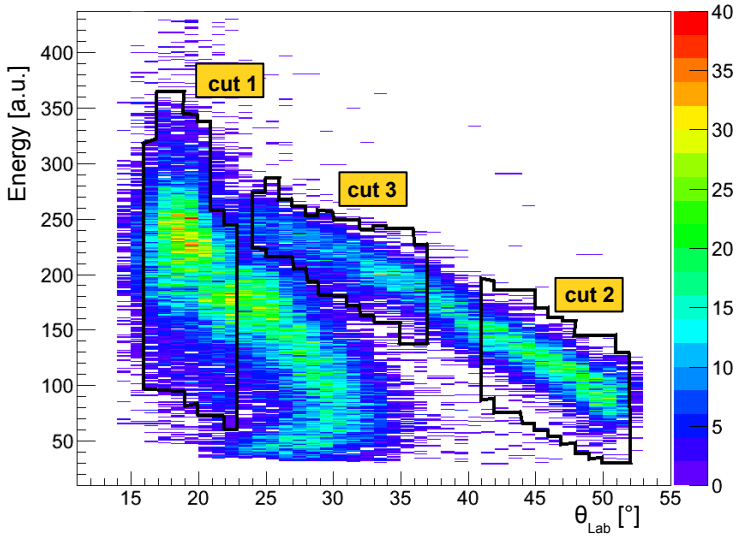


Figure 6.12.: Hits on the DSSSD according to the scattered particles (lower left branch: projectile-like particles, upper right branch: ^{64}Zn). The different cuts are indicated (numeration as in Table 6.4).

agonal matrix element is large. Still the most likely values are determined to be $M_{22} = -0.27_{-1.76}^{open}$ eb for three cuts and $M_{22} = -0.69_{-1.60}^{+3.61}$ eb for two cuts.

6.2.2 Details on ^{128}In

For the analysis of the 324 keV transition, knowledge of the spin and parity of the involved levels is needed. In [Hel03] a transition with such an energy is observed and suggested from comparison to shell model to be a deexcitation of either a 1^- or a 5^+ state to the 3^+ ground state of ^{128}In . Because the transition $1^- \rightarrow 3^+$ would have $M2$ character and magnetic excitations are highly suppressed in Coulomb excitation, the assumption of the excited state being a 5^+ -state is made, which has $E2$ character. Hence, the involved levels in the Coulomb excitation process are the 3^+ ground state and a 5^+ excited state. Thus the cross section depends on three matrix elements - the two diagonal ones (M_{33} and M_{55}) and the transitional matrix element M_{35} . For the maximum likelihood analysis two distinct cuts were

Table 6.4.: γ -ray yields for the transition $2_1^+ \rightarrow 0_{gs}^+$ in ^{128}Cd (N_γ^{proj}) and ^{64}Zn (N_γ^{targ}) in the different angular ranges (Θ_{cm}) after time gate subtraction, efficiency correction and background subtraction.

cut	$\Theta_{\text{cm}} [^\circ]$	Detected particle	N_γ^{proj}	N_γ^{targ}
1	49.5 – 74.4	projectile	333.3 (274)	698.4 (722)
2	76 – 98	target	281.5 (252)	679.2 (702)
3	106 – 132	target	126.1 (169)	321.4 (477)

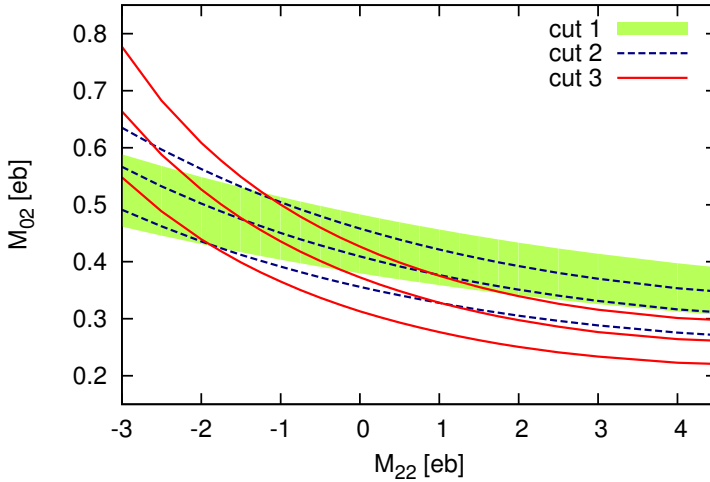


Figure 6.13.: Bands for the different angular ranges in the M_{02} - M_{22} -plane for ^{128}Cd .

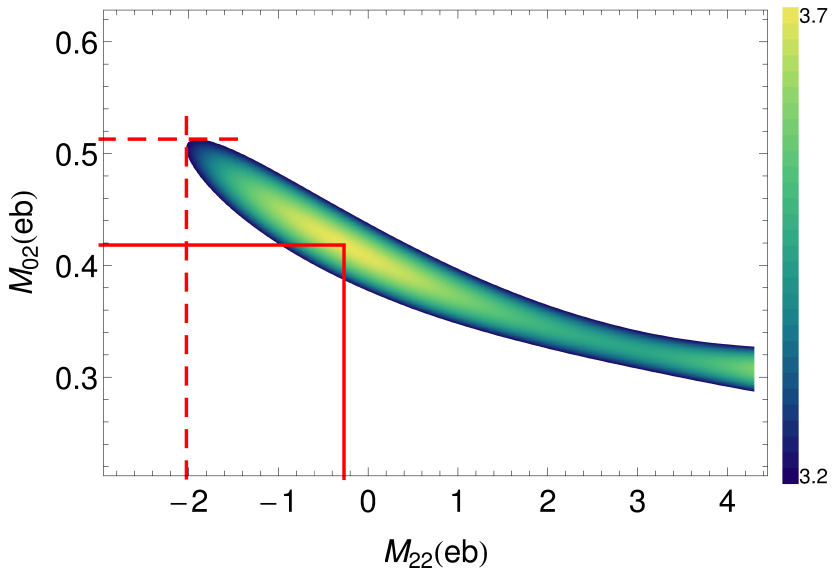


Figure 6.14.: 1σ -contour of the maximum likelihood analysis for the $0_{gs}^+ \rightarrow 2_1^+$ -transition in ^{128}Cd using three different particle angular ranges. The red lines indicate the maximum likely value (solid) and its errors (dashed).

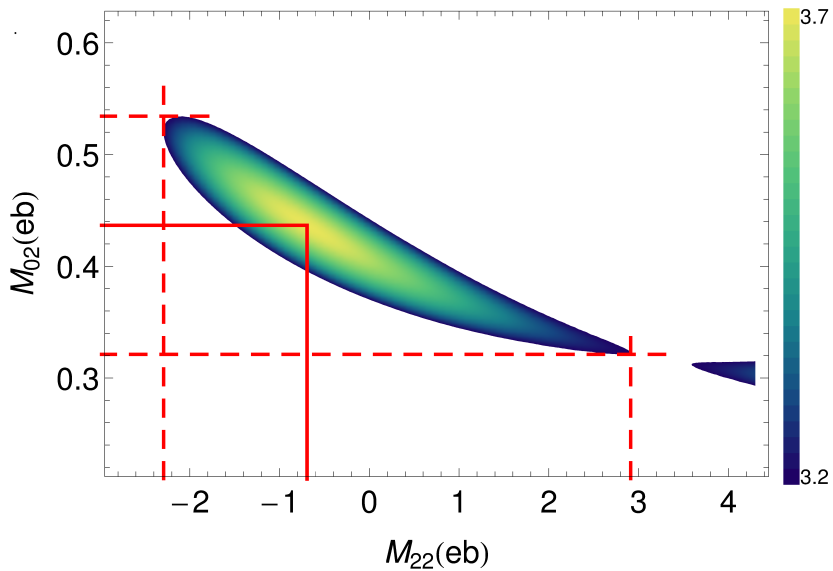


Figure 6.15.: 1σ -contour of the maximum likelihood analysis for the $0_{gs}^+ \rightarrow 2_1^+$ -transition in ^{128}Cd using only cut 1 and cut 3 (see Tab. 6.4). The red lines indicate the maximum likely value (solid) and its errors (dashed).

Table 6.5.: γ -ray yields for the transition $5_1^+ \rightarrow 3_{gs}^+$ in ^{128}In (N_γ^{proj}) and ^{64}Zn (N_γ^{targ}) in the different angular ranges (Θ_{cm}) after time gate subtraction, efficiency correction, background subtraction and correction for electron conversion.

cut	$\Theta_{\text{cm}} [^\circ]$	Detected particle	N_γ^{proj}	N_γ^{targ}
I	76 – 98	target	183.2(177)	681.9(440)
II	100 – 132	target	112.5(149)	448.9(370)

used, as shown in fig. 6.16. Similar to the analysis of ^{128}Cd a placement of a third cut causes the ellipse not to close for large positive M_{55} . The corresponding information on the γ -ray yield is given in Table 6.5. With Equation 6.1 the Coulomb excitation cross section for ^{128}In is calculated. From a previous measurement on the quadrupole moment of ground and isomeric states in neutron-rich In isotopes up to ^{126}In [Ebe86], a diagonal matrix element of $M_{33} = 0.3621$ eb ($Q_s(3^+) = 0.280$ eb) is estimated for the performed calculations. Nevertheless the impact of this diagonal matrix element on the B(E2)-value is rather small and calculations with a vanishing M_{33} give similar results. The matrix element M_{55} is varied between values of -8 eb and 4 eb. In figure 6.17 the obtained bands in the M_{35} - M_{55} -plane are shown. The 1σ contour (fig. 6.18) includes the errors from statistics, efficiency correction and beam purity. The maximum value for the transition matrix element is $M_{35} = 0.69_{-0.12}^{+0.13}$ eb for $M_{33} = 0.3621$ eb and $M_{35} = 0.68_{-0.12}^{+0.13}$ eb for vanishing M_{33} , which leads to the reduced transition strength $B(E2; 3_{gs}^+ \rightarrow 5^+) = 0.07_{-0.02}^{+0.03} e^2 b^2$ for $Q_s(3^+) = 0.280$ eb and vanishing $Q_s(3^+)$. The error for the diagonal matrix element M_{55} is large, but nevertheless the maximum likely value reads $M_{55} = -3.5_{-3.2}^{+5.0}$ eb for both cases of M_{33} , which gives $Q_s(5^+) = -2.5_{-2.3}^{+3.6}$ eb.

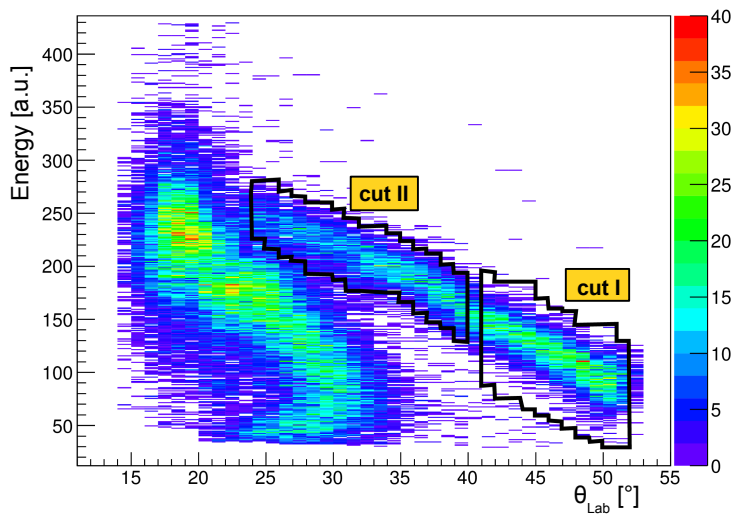


Figure 6.16.: Hits on the DSSSD according to the scattered particles (left branch: ^{128}Cd + decay products, right branch: ^{64}Zn). The different cuts are indicated (numeration as in Table 6.5).

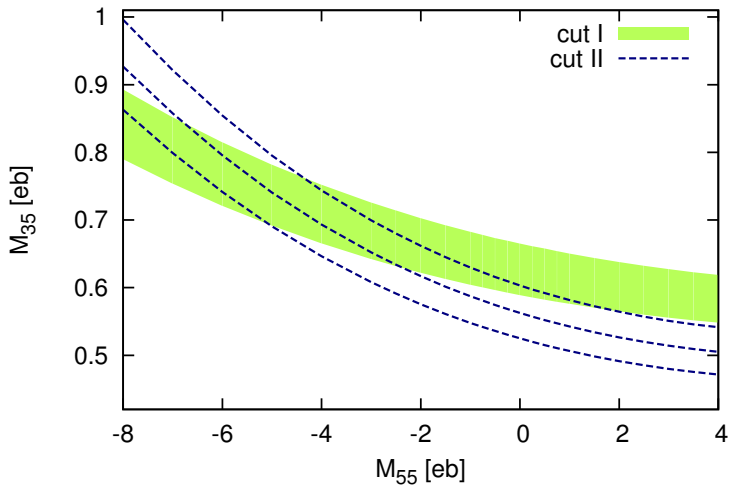


Figure 6.17.: Bands for the different angular ranges in the M_{35} - M_{55} -plane for ^{128}In with $M_{33} = 0.3621$ eb.

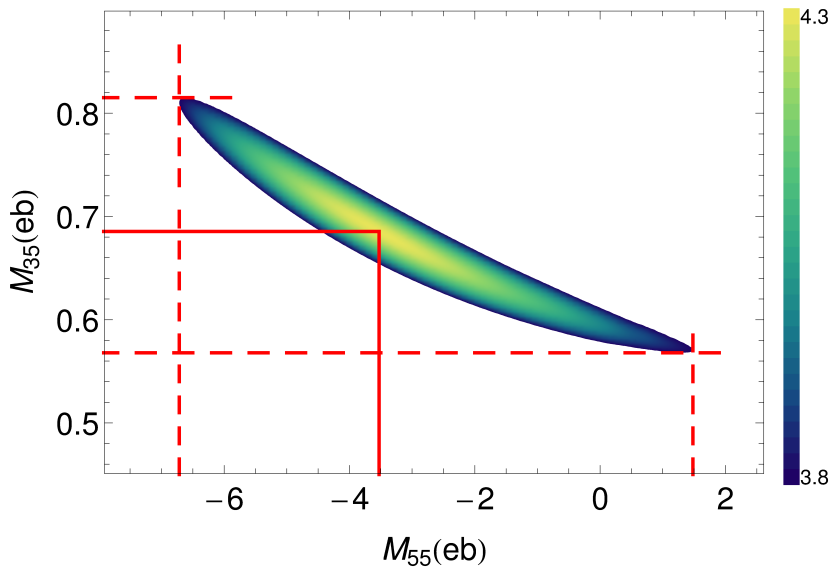


Figure 6.18.: 1σ -contour of the maximum likelihood analysis for the $3_{gs}^+ \rightarrow 5_1^+$ -transition in ^{128}In using $M_{33} = 0.3621$ eb. The red lines indicate the maximum likely value (solid) and its errors (dashed).

7 Results, discussion and outlook

7.1 Results and discussion

In Table 7.1 the experimental results for the reduced transition strength $B(E2; 0_{gs}^+ \rightarrow 2_1^+)$ and the spectroscopic quadrupole moment $Q_s(2_1^+)$ for ^{128}Cd together with the theoretical predictions from SM and BMF are summarised.

For the shell model calculations two different interactions were used: *jj45a* [Hjo] and *Napoli* [Cor02, Cov, Gen03, Sch04]. Both interactions are derived from nucleon-nucleon potentials, *jj45a* using the charge-dependent CD-Bonn [Mac01] and *Napoli* using the $V_{\text{low-k}}$ potential [Bog02]. The *jj45a* effective interaction is renormalised with Brückners G-matrix theory, which accounts for the short-range correlations [Hjo95, Mau13]. To obtain the $V_{\text{low-k}}$ potential, the high momentum components of a general nucleon-nucleon potential are integrated out by introducing a momentum cutoff $\Lambda = 2.0 \text{ fm}^{-1}$ [Bog02]. The calculation of the electric matrix elements is performed with the effective charges $e_\pi = 1.35$ and $e_\nu = 0.78$. The configuration space used for both interactions is based on a ^{78}Ni core. Therefore the orbits $\nu(1g_{7/2}, 1h_{11/2}, 2d_{3/2}, 2d_{5/2}, 3s_{1/2})$ for neutrons and $\pi(1f_{5/2}, 1g_{9/2}, 2p_{1/2}, 2p_{3/2})$ for protons are included.

For the beyond mean field calculations the finite range Gogny interaction in the D1S parametrisation is used [Ber84]. The crucial point for this interaction is the inclusion of a density dependence, which overcomes the problem of divergencies for the pairing interactions [Ben03, Ber84]. In order to restore the symmetries, particle number and angular momentum projection before the variation is applied. Furthermore a configuration mixing within the framework of the generator coordinate method, which is based on the collective model, has been performed [Rod08, Tab72]. The Gogny interaction is derived from global properties of nuclear matter and is therefore not restricted to a particular range of neutron or proton numbers. Calculations have been performed with and without the triaxial degree of freedom. Figure 7.1 shows the calculated 2_1^+ excitation energies in comparison with the experimental data. The absolute value for axially symmetric nuclei is by a factor of 1.7 too large, whereas it is reduced for the calculations including triaxiality. The trend of an increasing excitation energy of the 2_1^+ state for ^{122}Cd to ^{126}Cd and the following drop from ^{126}Cd to ^{128}Cd is better reproduced

Table 7.1.: Results of the Coulomb excitation experiment of ^{128}Cd compared with theoretical predictions from SM and BMF calculations for the $B(E2, 0^+_{gs} \rightarrow 2^+_1)$ and $Q_s(2^+_1)$ values. (* $Q_s(2^+_1)$ values kept fix in these columns.)

	Experiment			Shell Model		Beyond Mean Field		
	2 cuts	3 cuts	all	all	jj45a	Napoli	axial	triax
$B(E2)$ [e^2b^2]	0.19(9)	$0.17^{+0.09}_{-0.08}$	$0.16^{+0.03}_{-0.05}$ (0*)	0.18(3)	0.134	0.119	0.199	0.214
Q_s [eb]	$-0.5^{+2.7}_{-2.3}$	$-0.28^{+0.08}_{-1.7}$	(0*)	(-0.368*)	-0.013	-	-0.415	-0.368

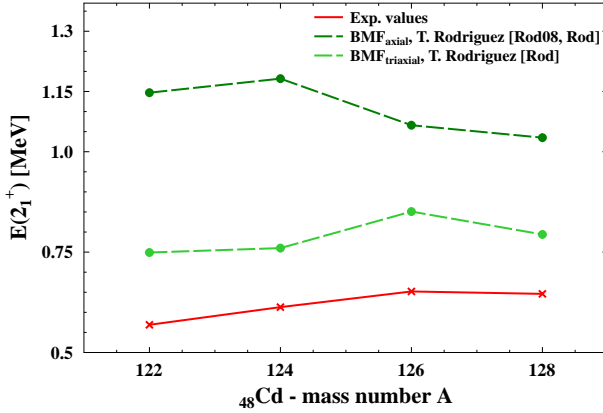


Figure 7.1.: Excitation energies of the 2_1^+ state in $^{122,124,126,128}\text{Cd}$ from experiment and BMF calculations with and without the triaxial degree of freedom [Rod].

for the latter case. A preference of a prolate shape is clearly evidenced in the calculated square amplitudes of the wave functions. Figure 7.2 shows a pronounced maximum for positive deformation parameter β for the 2_1^+ state. Additionally the calculated single particle energies (fig. 7.3) indicate a prolate deformation as the $\pi g_{9/2}$ and the $\nu h_{11/2}$ shell are closed for $\beta < -0.15$ and $\beta < -0.1$, respectively. Furthermore the formation of a 2^+ state would require a coupling to orbitals above the proton and neutron shell closures, which are very far away in energy from the closed shells. The deformation of a nucleus with closed proton and neutron shells needs a lot of energy. Therefore, from the BMF calculations, a prolate deformation is predicted. The triaxial degree of freedom γ does not affect the $B(E2)$ and $Q_s(2_1^+)$ value much. Figure 7.4 shows the collective wave functions in the triaxial plane for the ground and the first excited 2^+ state of ^{128}Cd . A clear maximum at $\gamma = 0^\circ$ and $\beta \sim 0.15$ and ~ 0.20 , respectively, is noted.

Figure 7.5 shows the evolution of the reduced transition strength from ^{122}Cd to ^{128}Cd for the experimental data and theoretical calculations. The general trend of an underestimation of the transition strength by SM calculations continues for ^{128}Cd , although the $N = 82$ shell closure gets closer. However, because of the

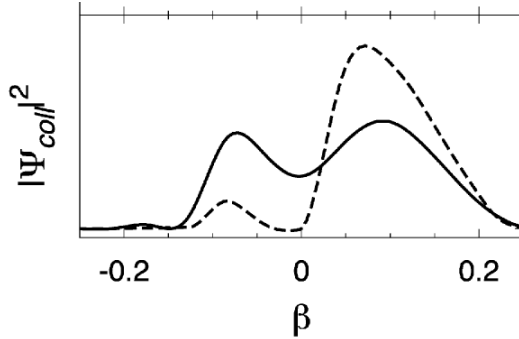


Figure 7.2.: Squared amplitudes of the wave functions from BMF calculations with respect to the deformation parameter β for the $J = 0$ ground state (solid) and $J = 2$ excited state (dashed). Taken from [Rod08].

large experimental uncertainty neither the BMF nor the SM calculations can be undoubtedly ruled out as an adequate theoretical description. In the vicinity of the BMF calculations, which is nevertheless favoured by experimental data, the enhanced transition strength can be explained with the large overlap of the ground state and excited state wave functions, as seen in figure 7.4.

The most likely value for the spectroscopic quadrupole moment is negative, which corresponds to prolate deformation and is in agreement with the theoretical predictions of both approaches. Recent results on the investigation of neutron-rich odd Cd isotopes with laser spectroscopy reveal small quadrupole moments for the ground states [Yor13]. Therefore, only a slight deformation is reasonable for the excited state of the even neutron-rich Cd isotopes. Nevertheless, the errorbars for this observable are too large to make an incontrovertible statement about the character of deformation.

In conclusion, the low energy Coulomb excitation experiment performed at REX-ISOLDE allowed for the extraction of the reduced transition strength of the $0_{gs}^+ \rightarrow 2_1^+$ transition. The enhanced value seems to follow the predictions of BMF calculations, although the SM can not be ruled out. Therefore no clear evidence could be found for shell gap quenching and theoretical extrapolations to nuclei involved in the r-process in this region still need to be taken with caution.

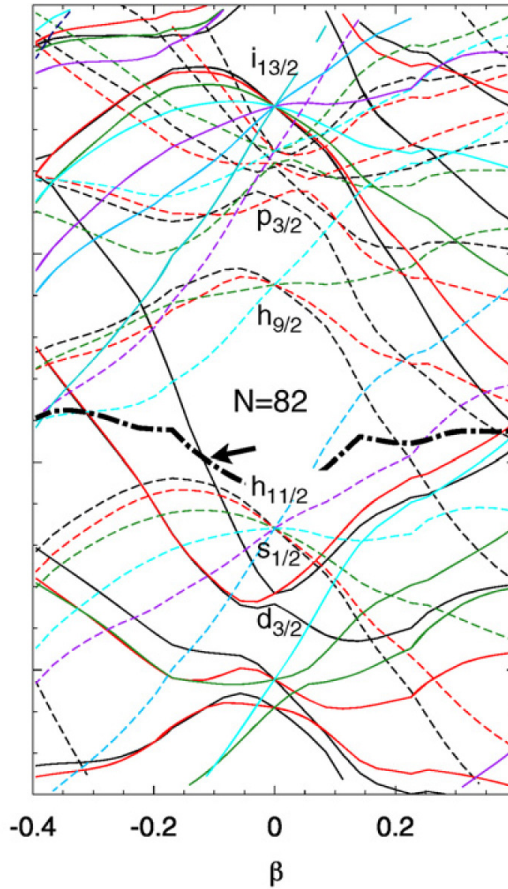


Figure 7.3.: Neutron single particle energies (shifted by 9 MeV) with respect to the deformation parameter β . The Fermi level is indicated (thick black dashed-dotted). Taken from [Rod08].

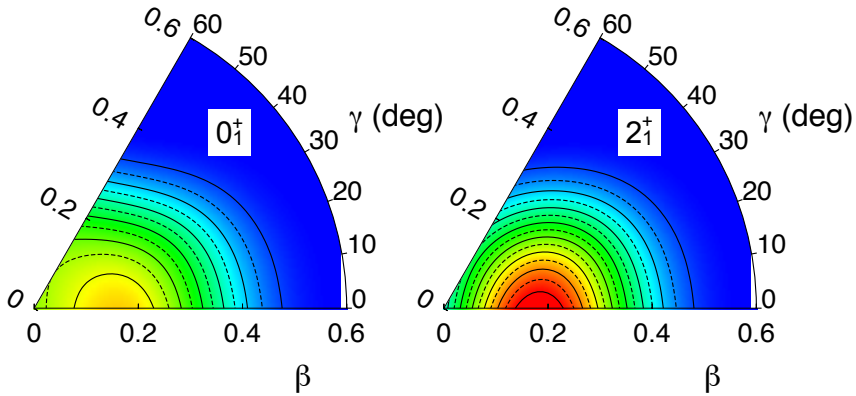


Figure 7.4.: Wave function of the ground state (left) and excited state (right) in the triaxiality plane. [Rod]

7.2 Outlook

Previous analyses of Coulomb excitation data revealed a large influence of additional information on the error of the extracted transition strength and quadrupole moment [Ili14]. In particular lifetime measurements of the excited state together with the information from Coulomb excitation reduce the error in the observables significantly. A lifetime measurement of the first excited 2^+ state of ^{128}Cd could therefore be helpful in order to affirm one of the discussed theories for this region undoubtedly. The lifetime calculated from the $B(E2)$ -values in chapter 7.1 lies roughly around 19-23 ps and is therefore accessible via the recoil-distance-doppler-shift method. There the beam hits a thin target foil and gets excited before hitting a stopper target. The deexcitation of the nuclei takes place in-flight and in the stopper target depending on the distance of the stopper from the excitation target and the lifetime of the excited state. By comparing the intensities of the in-flight decay and decay of the stopped nuclei at different stopper target distances with respect to the excitation target, the lifetime of the excited state can be deduced. Nevertheless, the largest source of uncertainty in Coulomb excitation experiments of exotic nuclei is the low statistics mainly due to low beam intensity. In order to extract the transition strength and quadrupole moments with a reasonable error higher intensities are indispensable. These can be reached by an upgrade of the target station, which is part of the HIE-ISOLDE project. Within this project also a

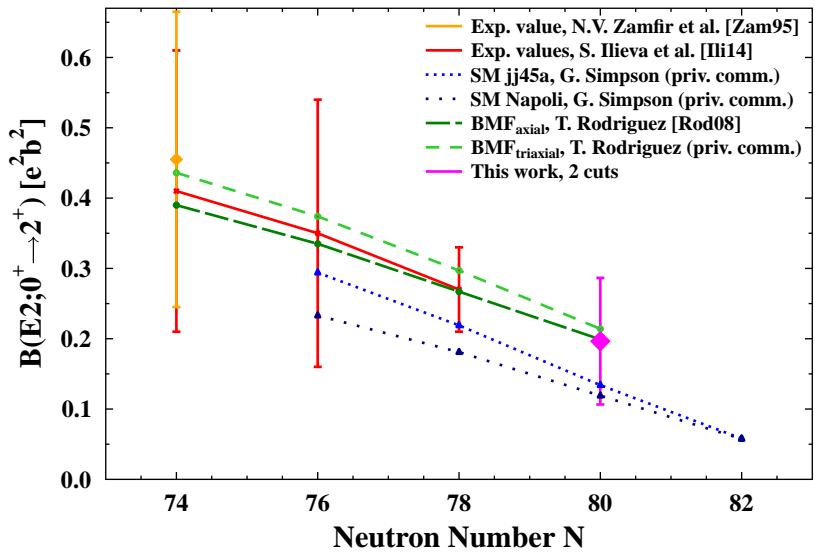


Figure 7.5.: Evolution of the reduced transition strength for neutron-rich Cd isotopes from experiment and theoretical calculations.

new linear accelerator will be installed, which will deliver beams with higher energies and will operate from 2015 on. More statistics in the γ -ray spectrum will be available and, hence, the uncertainty for the extracted results will be reduced. However, the upgrade will also embark new challenges as higher order effects like multistep Coulomb excitation complicate the analysis.

So far, it is not understood, where the enhanced collectivity (fig. 7.5) results from. The odd neutron-rich Cd isotopes represent an ideal probe to clarify the contributions from the different orbitals. With Coulomb excitation two different neutron states are accessible, as in the odd Cd isotopes ($A > 119$) besides the $\frac{3}{2}^+$ ground state there is an $\frac{11}{2}^-$ isomeric state present. The ground state wave function is dominated by the $d_{3/2}$ orbit, whereas the wave function of the isomeric state is dominated by the $h_{11/2}$ orbit. As ISOLDE provides a beam composed of ground state and isomeric state isotopes, the odd Cd's can be excited to low-spin states with positive parity from the ground state and to high-spin states with negative parity from the isomeric state. In May 2012 the campaign started with a Coulomb excitation experiment of ^{123}Cd performed at REX-ISOLDE, using the same setup as described in chapter 4. The relative amount of ground state and isomeric state of ^{123}Cd in the beam was varied with RILIS in order to assign the different transitions to ground state or isomeric state excitation. In this first attempt of the experiment only a broad-band laser was applicable, which limits the selectivity. Nevertheless, even with this broad-band laser the relative amount of isomeric state in the beam could be altered. The γ -spectrum revealed contradictions to the one measured via γ -spectroscopy after β -decay of ^{123}Ag by Huck et al. [Huc89]. In 2009 mass measurements at JYFLTRAP [Kan13] already found the isomeric state of ^{123}Cd at a different energy than Huck et al. [Huc89]. Therefore, with γ - γ -coincidence spectra from the Coulomb excitation experiment and the different laser settings, the levelscheme of ^{123}Cd could be revised (fig. 7.6, [Har14]). For the strongest transitions in the ground state band ($117\text{ keV}, 3/2_{gs}^+ \rightarrow 1/2_1^+$) and in the isomeric state band ($376\text{ keV}, 11/2^- \rightarrow 9/2^-$) the reduced transition matrix elements could be extracted as $M_{3/2 \rightarrow 1/2} = 0.92(4)\text{ eb}$ and $M_{11/2 \rightarrow 9/2} = 0.50(4)\text{ eb}$ [Har14]. These values are comparable and the conclusion can be drawn, that both the $d_{3/2}$ and the $h_{11/2}$ orbit contribute equally to the collectivity in the neutron-rich Cd isotopes. Further investigations with a narrowband laser for higher selectivity of the ground state and isomeric state isotope of ^{123}Cd and other neutron-rich odd Cd isotopes will shed more light onto the extraordinary region of doubly-magic ^{132}Sn .

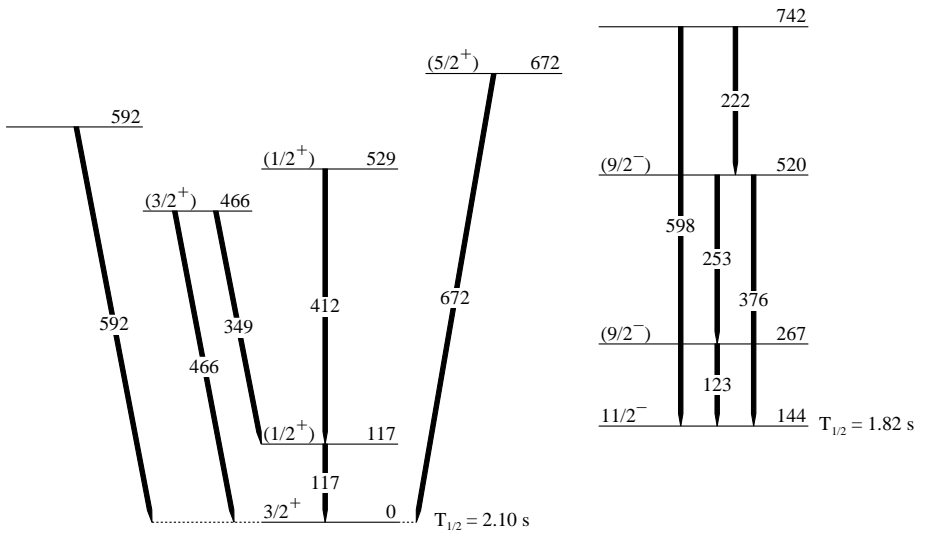


Figure 7.6.: Levelscheme of ^{123}Cd from [Har14].



A Kinematical reconstruction

To perform an even-by-event Doppler correction, the energy of the emitting particle needs to be known (equ. 5.5). If the detected particle is also the γ -ray emitting particle, the angle detected with the DSSSD can directly be inserted in the formulae:

Projectile p detected (A_p, Θ_p)

$$E_p = c_1 \left(\frac{A_t}{A_p + A_t} \right)^2 \left[1 + c_2 \cdot \left(\frac{A_p}{A_t} \right)^2 + 2\sqrt{c_2} \cdot \frac{A_p}{A_t} \cdot \cos \left(\Theta_p + \arcsin \left(\sqrt{c_1} \frac{A_p}{A_t} \sin(\Theta_p) \right) \right) \right] \quad (\text{A.1})$$

Target t detected (A_t, Θ_t)

$$E_t = c_1 \frac{A_p A_t}{(A_p + A_t)^2} \left[1 + c_2 + 2\sqrt{c_2} \cdot \cos \left(\Theta_t + \arcsin \left(\sqrt{\frac{A_p A_t E_{beam}}{A_p A_t E_{beam} - \Delta E (A_p + A_t)}} \cdot \sin(\Theta_t) \right) \right) \right] \quad (\text{A.2})$$

with

$$\begin{aligned} c_1 &= A_p E_{beam} - \Delta E \left(1 + \frac{A_p}{A_t} \right) \\ c_2 &= \frac{A_p E_{beam}}{c_1} \end{aligned} \quad (\text{A.3})$$

where E_{beam} is the incoming beam energy and ΔE is the loss of kinetic energy in the inelastic scattering process, which equals the excitation energy.

If the γ -ray emitting nucleus is not detected but only its scattering partner, the scattering angle of the emitting nucleus needs to be reconstructed:

Projectile p detected (A_p, Θ_p)

$$\Theta_t = \arccos \left(\frac{p_0^2 + p_p^2 - 2A_p^2 E_{beam} - A_p^2 E_{beam}^2 + 2A_p E_{rec} + 2E_{beam} A_p E_{rec} - E_{rec}^2}{2p_0 p_p} \right) \quad (\text{A.4})$$

Target t detected (A_t, Θ_t)

$$\Theta_p = \arccos \left(\frac{p_0^2 - p_t^2 + p_p^2}{2p_0 p_p} \right) \quad (\text{A.5})$$

with

$$\begin{aligned} p_0 &= \sqrt{E_{beam}^2 A_p^2 + 2E_{beam} A_p^2} \\ p_t &= \sqrt{(E_{beam} A_p - E_{part} - \Delta E)^2 + 2A_p (E_{beam} A_p - E_{part} - \Delta E)} \\ p_p &= \sqrt{E_{rec}^2 + 2A_t E_{rec}} \\ E_{rec} &= E_{beam} A_p - E_{part} - \Delta E \end{aligned} \quad (\text{A.6})$$

where ‘‘part’’ is referring to the detected particle.

Note, that in the above considerations the energies and angles are meant as being in the laboratory system.

Bibliography

- [Alb13] M. Albers et al. *Nucl. Phys. A*, **899**:1–28, 2013.
- [Ald56] K. Alder et al. *Rev. of Mod. Phys.*, **28**, 1956.
- [Alk93] G.D. Alkhazov et al. *Z. Phys. A*, **344**:425–429, 1993.
- [Bar57] J. Bardeen et al. *Phys. Rev.*, **106**:162–164, 1957.
- [Bar13] B.R. Barrett et al. *Prog. in Part. and Nucl. Phys.*, **69**:131–181, 2013.
- [Ben03] M. Bender et al. *Rev. of Mod. Phys.*, **75**, 2003.
- [Ber84] J.F. Berger et al. *Nucl. Phys. A*, **428**:23c–36c, 1984.
- [Ber07] C.A. Bertulani. *Nuclear Physics in a Nutshell*. Princeton University Press, 2007.
- [Ber12] J. Beringer et al. *Phys. Rev. D*, **86**:010001:391, 2012.
- [Bet08] K. Bethge et al. *Kernphysik*. Springer-Verlag Berlin Heidelberg, 3. edition, 2008.
- [Bla52] J.M. Blatt and V.F. Weisskopf. *Theoretical Nuclear Physics*. John Wiley and Sons, New York, 1952.
- [Blo69] E.D. Bloom. *Phys. Rev. Lett.*, **23**:930–934, 1969.
- [Bog58] N.N. Bogoliubov. *Sov. Phys. JETP*, **7**:41, 1958.
- [Bog02] S. Bogner et al. *Phys. Rev. C*, **65**:051301, 2002.
- [Boh53] A. Bohr and B. Mottelson. *Mat. Fys. Medd. Dan. Vid. Selsk.*, **27**, 1953.
- [Boh58] A. Bohr and B.R. Mottelson. *K. Norske Viden. Selsk. Forh.*, **31**:12, 1958.
- [Bor25] M. Born and P. Jordan. *Zeitschrift für Physik*, **34**:858–888, 1925.
- [Bor26] M. Born et al. *Zeitschrift für Physik*, **35**:557–615, 1926.

-
- [Bot30] W. Bothe and H. Becker. *Zeitschrift für Physik*, **66**:289, 1930.
- [Bre56] G. Breit et al. *Phys. Rev.*, **103**:727, 1956.
- [Bre69] M. Breidenbach. *Phys. Rev. Lett.*, **23**:935–939, 1969.
- [Cha32] J. Chadwick. *Nature*, **129**:312, 1932.
- [Che95] B. Chen et al. *Phys. Lett. B*, **355**:37, 1995.
- [Cli69] D. Cline. *Bull. Am. Phys. Soc.*, **14**:726, 1969.
- [Cor02] L. Coraggio et al. *Phys. Rev. C*, **66**:064311, 2002.
- [Cov] A. Covello and A. Gargano. *private communication*.
- [Dan11] M. Danchev et al. *Phys. Rev. C*, **84**:061306(R), 2011.
- [Dec80] J. Dechargé and D. Gogny. *Phys. Rev. C*, **21**:1568, 1980.
- [Dob94] J. Dobaczewski et al. *Phys. Rev. Lett.*, **72**:981, 1994.
- [Ebe86] J. Eberz et al. *Nucl. Phys. A*, **464**:9–28, 1986.
- [Eis75] J.M. Eisenberg and W. Greiner. *Nuclear Theory 1 - Nuclear Models*. North-Holland Publishing Company, 2. edition, 1975.
- [Fed00] V.N. Fedoseyev et al. *Hyperfine Interactions*, **127**:409–416, 2000.
- [Fog79] B. Fogelberg and P. Carlé. *Nucl. Phys. A*, **323**:205–252, 1979.
- [Fog88] B. Fogelberg. *Nucl. Data for Science and Techn.*, pages 837–840, 1988.
- [Fra14] J. Fraunhofer. *Denkschriften der Königlichen Akademie der Wissenschaften zu München*, **5**:193–226, 1814.
- [Gaf12] L. Gaffney. *PhD Thesis*, 2012.
- [Gap32] E. Gapon and D. Ivanenko. *Die Naturwissenschaften*, **20**:792–793, 1932.
- [Gar08] P.E. Garrett et al. *Phys. Rev. C*, **78**:044307, 2008.
- [Gei09] H. Geiger and E. Marsden. *Proc. Roy. Soc. A*, **82**:495–500, 1909.
- [Gel64] M. Gell-Mann. *Phys. Lett.*, **8**:214–215, 1964.

-
- [Gen03] J. Genevey et al. *Phys. Rev. C*, **67**:054312, 2003.
- [Gla09] T. Glasmacher. *The Euroschool Lectures on Physics with Exotic Beams, Vol. III*. Springer-Verlag Berlin Heidelberg, 2009.
- [Goe49] M. Goeppert-Mayer. *Phys. Rev.*, **75**, 1949.
- [Goe55] M. Goeppert-Mayer and J.H.D. Jensen. *Elementary Theory of Nuclear Shell Structure*. WILEY, New York, 1. edition, 1955.
- [Gok86] H. Gokturk et al. *Z. Phys. A*, **324**:117, 1986.
- [Hab00] D. Habs et al. *Hyperfine Interactions*, **129**:43–66, 2000.
- [Har14] A.-L. Hartig. Coulomb-anregung von ^{123}Cd , Master thesis, 2014.
- [Hax49] O. Haxel, J.H.D. Jensen and H.E. Suess. *Phys. Rev.*, **75**, 1949.
- [Hei25] W. Heisenberg. *Zeitschrift für Physik*, **33**:879–893, 1925.
- [Hei32] W. Heisenberg. *Zeitschrift für Physik*, **77**:1–11, 1932.
- [Hel03] M. Hellström et al. Fission and Properties of Neutron-Rich Nuclei, pages 22–29, 2003.
- [Hes80] P.O. Hess et al. *Z. Phys. A*, **296**:147–163, 1980.
- [Hjo] M. Hjorth-Jensen. *unpublished*.
- [Hjo95] M. Hjorth-Jensen et al. *Physics Reports*, **261**:125–270, 1995.
- [Huc89] H. Huck. *Phys. Rev. C*, **40**:1384–1389, 1989.
- [Ili14] S. Ilieva et al. *Phys. Rev. C*, **89**:014313, 2014.
- [inc14] The Interactive Nuclear Chart - inch. <http://personal.ph.surrey.ac.uk/~phplc/Programs/Inch/inch.html>, as at April 2014.
- [Kan01] M. Kanbe et al. *Nucl. Dat. Sheets*, 94:227, 2001.
- [Kan13] A. Kankainen. *Phys. Rev. C*, **87**:024307, 2013.
- [Kau00] T. Kautzsch et al. *Eur. Phys. J. A*, **9**:201, 2000.
- [Ker74] A. Kerek et al. *Nucl. Phys. A*, **224**:367–395, 1974.

-
- [Kes03] O. Kester et al. *Nucl. Instr. and Meth. B*, **204**:20–30, 2003.
- [Kib08] T. Kibédi et al. *Nucl. Instr. and Meth. A*, **589**:202–229, 2008.
- [Kir60] G. Kirchhoff and R. Bunsen. *Annalen der Physik und der Chemie (Poggendorf)*, **110**:161–189, 1860.
- [Koi03] M. Koizumi et al. *JAERI Review*, **028**:22–23, 2003.
- [Krö07] Th. Kröll. *CERN-INTC-2007-013+INTC-P-226*, 2007.
- [Kug00] E. Kugler. *Hyperfine Interactions*, **129**:23–42, 2000.
- [Lea09] L. Cáceres et al. *Phys. Rev. C*, **79**:011301(R), 2009.
- [Lin04] M. Lindroos. Proc. of EPAC, pages 45–49, 2004.
- [Lis08] A.F. Lisetskiy et al. *Phys. Rev. C*, **78**:044302, 2008.
- [Mac86] H. Mach et al. *Phys. Rev. C*, **34**:1117–1119, 1986.
- [Mac01] R. Machleidt. *Phys. Rev. C*, **63**:024001, 2001.
- [Mar02] D.C.J. Marsden et al. *Phys. Rev. C*, **66**:044007, 2002.
- [Mau13] K. Maurya et al. *IOSR Journal of Applied Physics*, **3**:52–59, 2013.
- [Mut65] R. Muthukrishnan and M. Baranger. *Phys. Lett.*, **18**:2, 1965.
- [Nav00] P. Navrátil et al. *Phys. Rev. C*, **62**:054311, 2000.
- [Nie51] A.O. Nier et al. *Phys. Rev.*, volume =, 1951.
- [Nil55] S.G. Nilsson. *Mat. Fys. Medd. Dan. Vid. Selsk.*, **29**, 1955.
- [nob14] The Nobel Prize in physics 1963. http://www.nobelprize.org/nobel_prizes/physics/laureates/1963/, as at 9 Mar 2014.
- [Ost02] A.N. Ostrowski et al. *Nucl. Instr. and Meth. A*, **480**:448–455, 2002.
- [Pie11] S. Pietri et al. *Phys. Rev. C*, **83**:044328, 2011.
- [Rad02] D.C. Radford et al. *Phys. Rev. Lett.*, **88**:22, 2002.
- [Ram01] S. Raman et al. *At. Data. and Nucl. Data Tables*, **78**, 2001.

-
- [Rei87] P.-G. Reinhard and K. Goeke. *Rep. Prog. Phys.*, **50**:1–64, 1987.
- [Rei89] P.-G. Reinhard. *Rep. Prog. Phys.*, **52**:439–514, 1989.
- [Rod] T.R. Rodríguez. *private communication*.
- [Rod08] T.R. Rodríguez et al. *Phys. Lett. B*, **668**:410–413, 2008.
- [Rot07] R. Roth and P. Navrátil. *Phys. Rev. Lett.*, **99**:092501, 2007.
- [Rut11] E. Rutherford. *Philosophical Magazine*, **21**:669–688, 1911.
- [Sal88] S. Salém-Vasconcelos et al. *Phys. Rev. C*, **38**, 1988.
- [Sch04] A. Scherillo et al. *Phys. Rev. C*, **70**:054318, 2004.
- [Ste07] I. Stetcu et al. *Phys. Rev. Lett. B*, **653**:358, 2007.
- [Sto06] J.R. Stone and P.-G. Reinhard. *arXiv:nucl-th/0607002v1*, 2006.
- [Tab72] F. Tabakin. *Nucl. Phys. A*, **182**:497–521, 1972.
- [Val58] J.G. Valatin. *Nuovo Cimento*, **7**:843, 1958.
- [vW35] C.F. von Weizsäcker. *Zeitschrift für Physik*, **96**:431–458, 1935.
- [War13] N. Warr et al. *Eur. Phys. J. A*, **49**:40, 2013.
- [War14] N. Warr webpage. <http://www.ikp.uni-koeln.de/~warr/doc/index.html>, as at April 2014.
- [Wat13] H. Watanabe et al. *Phys. Rev. Lett.*, **111**, 2013.
- [Wig37] E. Wigner. *Phys. Rev.*, **51**:106–119, 1937.
- [Wol02] W.H. Wollaston. *Philosophical Transactions of the Royal Society*, **92**:365–380, 1802.
- [Woo54] R.D. Woods and D.S. Saxon. *Phys. Rev.*, **95**:577–578, 1954.
- [Yor13] D.T. Jordanov. *Phys. Rev. Lett.*, **110**:192501, 2013.
- [Yuk35] H. Yukawa. *Proc. Phys. Math. Soc. Japan*, **17**:48, 1935.
- [Zie04] J.F. Ziegler. *Nucl. Instr. and Meth. B*, **219**:1027–1036, 2004.
- [Zwe64] G. Zweig. *CERN Report*, **No.8419/TH.412**, 1964.



List of Figures

1.1. Nuclear chart	4
1.2. Part of the nuclear chart	5
1.3. Excitation energies for the 2_1^+ state in different isotopes	5
2.1. Schematic view of excitation energies for vibrational and rotational nuclei	9
2.2. Sketch of square well, oscillator and Woods-Saxon potential	11
2.3. Shell model levels for harmonic oscillator and Woods-Saxon potential	13
2.4. Nilsson levels	16
3.1. Schematic view of low-energy Coulomb scattering	20
3.2. Excitation mechanisms of first and second order	24
4.1. Schematic view of the extraction process of nuclei at ISOLDE using a resonant laser ion source	28
4.2. 3-step excitation scheme of ^{128}Cd	29
4.3. Schematic view of REX	29
4.4. Sketch of the timing structure at REX-ISOLDE	32
4.5. Picture and dimensions of the DSSSD	33
4.6. Sketch of the $\Delta E - E$ telescope	34
4.7. MINIBALL detector array	34
4.8. Sketch of a 6-fold segmented HPGe cluster detector	35
5.1. Distance of closest approach D_{\min} for ^{128}Cd nuclei scattered at ^{64}Zn	38
5.2. Coulomb excitation cross section for $0_{gs}^+ \rightarrow 2_1^+$ transition in ^{64}Zn and ^{128}Cd	39
5.3. Scattering kinematics of $^{64}\text{Zn}(^{128}\text{Cd}, ^{128}\text{Cd}^*)^{64}\text{Zn}^*$	40
5.4. Relative efficiency of the MINIBALL detector array	41
5.5. DSSSD hit pattern	43
6.1. Particle- γ coincidence spectrum	46
6.2. $\Delta E - E_{\text{rest}}$ plot	48

6.3. Doppler corrected γ -spectra for the first 5:45h and the last 9:42h of the experiment	49
6.4. ΔE -T plot	50
6.5. γ -ray spectrum after β -decay of the beam implanted in a thick ^{64}Zn target	51
6.6. Levelscheme of ^{128}In	52
6.7. Partial level scheme of ^{128}Sn after β -decay of ground state ^{128}In	54
6.8. Partial level scheme of ^{128}Sn after β -decay of isomeric ^{128m}In	56
6.9. Background subtracted $\gamma\gamma$ -coincidence spectra	58
6.10. Prompt Doppler corrected γ -ray spectrum	61
6.11. Procentual change in the differential cross section	62
6.12. Implied cuts for ^{128}Cd	65
6.13. Bands for the different angular ranges in the M_{02} - M_{22} -plane for ^{128}Cd	66
6.14. 1σ -contour of the maximum likelihood analysis for the $0_{gs}^+ \rightarrow 2_1^+$ - transition in ^{128}Cd using 3 cuts	67
6.15. 1σ -contour of the maximum likelihood analysis for the $0_{gs}^+ \rightarrow 2_1^+$ - transition in ^{128}Cd using 2 cuts	68
6.16. Implied cuts for ^{128}In	70
6.17. Bands for the different angular ranges in the M_{35} - M_{55} -plane for ^{128}In	71
6.18. 1σ -contour of the maximum likelihood analysis for the $3_{gs}^+ \rightarrow 5_1^+$ - transition in ^{128}In	72
7.1. Excitation energies of the 2_1^+ state in $^{122,124,126,128}\text{Cd}$ from experiment and BMF calculations	75
7.2. Squared amplitudes of the wave functions from BMF calculations	76
7.3. Neutron single particle energies	77
7.4. Wave function of the ground state and excited state in the triaxiality plane	78
7.5. Evolution of the reduced transition strength for neutron-rich Cd isotopes	79
7.6. Levelscheme of ^{123}Cd	81

List of Tables

5.1. Angular coverage of the DSSSD	43
6.1. Relative γ -ray intensities for ^{128}In	53
6.2. γ -ray intensities for ^{128}Sn after ground state ^{128}In decay	55
6.3. Relative γ -ray intensities for ^{128}Sn from isomeric state ^{128}In	59
6.4. γ -ray yields for the transition $2_1^+ \rightarrow 0_{\text{gs}}^+$ in ^{128}Cd	66
6.5. γ -ray yields for the transition $5_1^+ \rightarrow 3_{\text{gs}}^+$ in ^{128}In	69
7.1. Results for ^{128}Cd compared with theoretical predictions	74

List of Publications

- C. Bauer et al., *Phys. Rev. C* **88**, 021302(R) (2013)
- N. Warr et al., *The Eur. Phys. J. A* **49**, 40 (2013)
- L.P. Gaffney et al., *Nature* **497**, 7448 (2013)
- C. Bauer et al., *Phys. Rev. C* **00**, 001300(R) (2013)
- T. Grahn et al., *EPJ Web of Conferences* **63**, 01009 (2013)
- S. Bönig et al., *EPJ Web of Conferences* **66**, 02012 (2014)
- A. Jungclaus et al., *EPJ Web of Conferences* **66**, 02040 (2014)
- M. von Schmid et al., *EPJ Web of Conferences* **66**, 03093 (2014)
- S. Ilieva et al., *Phys. Rev. C* **89**, 014313 (2014)
- J. Taprogge et al., *Phys. Rev. Lett.* **112**, 132501 (2014)

Curriculum Vitae

Personal Information

Name: Esther Sabine Bönig
Address: Havelstrasse 22, 64295 Darmstadt
Date of Birth: 25. Februar 1986
Place of Birth: Bünde, Germany
Nationality: German
Parents: Marion Bönig, née Schröder
Günter Bönig

Education

June 2013:

Best Young Poster Award at International nuclear physics conference, Firenze, Italy

Since November 2010:

PhD student in physics at Technische Universität Darmstadt, Germany
Supervisor: Prof. Dr. Thorsten Kröll

October 2008 – October 2010:

Masterstudent in physics at University of Bielefeld, Germany
Degree: Master of Science (October 2010)
Title of the Master Thesis: "*Soft-Collinear Effective Theory*"
Supervisor: Junior-Prof. Nicolas Borghini, PhD

August 2009 – December 2009:

Exchange student in physics at University of Jyväskylä, Finland

Oktober 2005 – September 2008:

Bachelorstudent in physics at University of Bielefeld, Germany

Degree: Bachelor of Science (September 2008)

Title of the Bachelor Thesis: "*Relativistische Effekte in der Sternbeobachtung*"

Supervisor: Prof. Dr. Dominik Schwarz

August 1996 – June 2005:

Gymnasium at Gymnasium am Markt, Bünde, Germany

Degree: Abitur

August 1992 – June 1996:

Primary School at Grundschule Eilshausen, Germany